Object-based landfast sea ice detection over West Antarctica using time series ALOS PALSAR data

Miae Kim[a,b,c], Hyun-Cheol Kim[d], Jungho Im[a,*], Sanggyun Lee[e], Hyangsun Han[f]

[a] School of Urban and Environmental Engineering, Ulsan National Institute of Science and Technology (UNIST), Ulsan 44919, South Korea
[b] Institute of Meteorology and Climate Research, Karlsruhe Institute of Technology, 76128 Karlsruhe, Germany
[c] Institute of Photogrammetry and Remote Sensing, Karlsruhe Institute of Technology, 76128 Karlsruhe, Germany
[d] Unit of Arctic Sea-Ice Prediction, Korea Polar Research Institute, Incheon 21990, South Korea
[e] Centre for Polar Observation and Modelling, Earth Sciences, University College London, London WC1E 6BS, UK
[f] Division of Geology & Geophysics, Kangwon National University, Chuncheon, Gangwon-do 24341, South Korea

ARTICLE INFO

ABSTRACT

Landfast sea ice (fast ice) is an important feature prevalent around the Antarctic coast, which is affected by climate change and energy exchanges with the atmosphere and ocean. This study proposed a method for detection of the West Antarctic fast ice using the Advanced Land Observing Satellite Phased Array L-band SAR (ALOS PALSAR) images. The algorithm has combined image segmentation, image correlation analysis, and machine learning techniques (i.e., random forest (RF), extremely randomized trees (ERT), and logistic regression (LR)). We used SAR images with a baseline of 5 days that are not in the same orbit but overlap each other as overlaps between swaths in adjacent orbits are often available in the polar regions. The underlying assumption for the proposed fast ice detection algorithm is that fast ice regions in SAR images with a time interval of 5 days are highly correlated. The object-based approach proposed in this study was well suited to high-resolution SAR images in deriving spatially homogeneous fast ice regions. The image segmentation results using the optimized parameters showed a distinct difference in the backscatter temporal evolution between fast ice and pack ice regions. Correlation and STD of backscattering coefficients were found to be the most significant variables for the object-based fast ice detection from two temporally separated images. In overall, the quantitative and qualitative evaluation demonstrated that the algorithm was an effective approach to detect fast ice with high accuracies. The models well detected various fast ice regions in the West Antarctica but misclassified some objects. The misclassifications occurred toward the edge of fast ice regions with relatively rapid changes in backscattering between both data acquisitions. On the other hand, few fast ice objects were misclassified as uniform backscattering over time occurred by chance on very small objects far from the coast. Very old multi-year fast ice regions with high backscattered signals were also a source for some misclassifications. This may be due to the sensitivity of L-band to snow structure to some extent and a thinner ice over the region with either ice growth (no deformation) or closing (slight deformation) between both images. Heavy snow load on the ice could be another error source for some misclassification as well. The approach allowed for the reliable detection of fast ice regions by using L-band SAR images with a small local incidence angle difference.

1. Introduction

Sea ice plays an important role in modulating global climate and ocean changes by reflecting incoming solar radiation (Parkinson and DiGirolamo, 2016) and decreasing heat loss from the ocean to the atmosphere (Stammerjohn et al., 2008). Antarctic sea ice production also contributes to deep-water formation and hence affects global atmospheric and thermohaline ocean circulation (Zwally et al., 1983;

Bintanja et al., 2013; Ohshima et al., 2013). Sea ice conditions including extent, concentration, thickness, and deformation have practical implications on scientific exploration and research such as ice navigation and route planning for icebreakers, and in situ sampling strategy (Parkinson and Cavalieri, 2012; Normile, 2015). The Antarctic sea ice extent has shown a slowly increasing trend while Arctic sea ice extent has diminished (Zwally et al., 2002; Cavalieri and Parkinson, 2008; Simmonds, 2015; Parkinson and DiGirolamo, 2016; Comiso et al.,

2017). However, more recently a significant decrease of the sea ice extent was observed over the Antarctic Ocean (Turner et al., 2017; Viñas, 2017). This demonstrates the importance to continuously monitor the sea ice extent to determine the long-term trend in Antarctic sea ice and to identify any causality in global warming.

This study focuses on landfast sea ice (hereafter fast ice) regions in the nearshore sea ice zone in the Antarctica. Fast ice forms along coastlines and is fastened to ice walls, ice fronts, or icebergs with little motion (WMO, 2014). Fast ice can form from the seawater in place or by the freezing of floating ice of any age. Fraser et al. (2012) showed that fast ice is prevalent throughout the spring season along the East Antarctic coast. With the help of icebergs as anchor points, it can extend to hundreds of kilometers far from the coast (Massom et al., 2001). While fast ice regions occupy a small fraction of the sea ice extent in the East Antarctica, its volume constitutes a higher proportion of the sea ice volume (Giles et al., 2008). Thick sea ice often happens in the fast ice zone (Kurtz and Markus, 2012; Price et al., 2013; Xie et al., 2013; Kern et al., 2016). The distribution of fast ice affects the shape and size of polynyas; 13% of Southern Ocean sea ice production takes place in the major Antarctic coastal polynyas (Tamura et al., 2008; Fraser et al., 2019). Then, dense water forms through brine rejection during sea ice formation, which is a source of the Antarctic Bottom Water (Ohshima et al., 2013; Nihashi and Ohshima, 2015). Fast ice can delay ice-shelf calving and indirectly affect ice sheet mass balance (Massom et al., 2010). Fast ice is also significant in providing extensive habitats and breeding places for microorganisms, Emperor penguins, and Weddell seals (Massom et al., 2009).

Although continuous efforts of monitoring fast ice have been made through in-situ measurements (Murphy et al., 1995; Ushio, 2006; Heil, 2006), it is difficult to obtain long-term in situ measurements over vast areas. In-situ measurements for fast ice are generally limited to fixed locations where ice is thick enough for sampling. Satellite remote sensing provides an alternative method for fast ice observations as it produces data covering substantial areas with good temporal resolution. A variety of fast ice studies have been conducted in polar regions (Fraser et al., 2012; Mahoney et al., 2014; Nihashi and Ohshima, 2015; Dammann et al., 2019). In Antarctica, studies have been mainly limited to the East Antarctic coast using satellite remote sensing such as detection of fast ice extent, estimation of its thickness, and analysis of its long-term distribution and variability (Massom et al., 2009; Fraser et al., 2010; Giles et al., 2011; Fraser et al., 2012; Han et al., 2015; Yang et al., 2016; Li et al., 2018). Nihashi and Ohshima (2015) conducted circumpolar mapping of fast ice using AMSR-E images, but the fast ice extent was considerably underestimated when compared to MODIS-derived fast ice maps (Fraser et al., 2019).

Optical sensor images can be useful for classifying fast ice and pack ice regions. However, they do not provide surface information when clouds are present. As clouds are often present (approximately 60–80% cloud cover depending on location and season) in Antarctica (Comiso and Steffen, 2001; Spinhirne et al., 2005; Suen et al., 2014; Scott et al., 2017), optical sensors might not provide the best solution to fully monitor fast ice regions. Considering the effect of cloud contamination, previous studies have detected fast ice using optical sensor data by compositing images with dozens of days (Fraser et al., 2010; Fraser et al., 2012). Such an approach is appropriate for relatively stable and large fast ice areas, but may not be suitable for rapidly changing fast ice regions where ice break-ups and (re)-growth occur frequently. Fast ice changes at short timescales are an important factor for the Antarctic coastal system, as fast ice physically interacts with ice tongues and also affects the polynya regions (Giles et al., 2008). Some fast ice regions can be in environmentally dynamic conditions due to varied sea ice drift patterns and ocean currents, which could lead to changes in fast ice (Meyer et al., 2011).

Passive or active microwave sensors have the advantage of providing images regardless of solar illumination or weather conditions. Meanwhile, passive microwave data have relatively coarse spatial

resolution (~3–50 km), limiting their applications to wide fast ice regions near the shoreline. Synthetic aperture radar (SAR), an active microwave sensor, can be a powerful instrument for fast ice research because it can observe sea ice in high spatial resolution. SAR sensors at L-, C-, and X-bands have been used for classification of sea ice types since backscattered radar intensity is dependent on surface roughness and sea ice properties (Karvonen, 2004; Zakhvatkina et al., 2013; Liu et al., 2015; Ressel et al., 2015; Wang et al., 2016; Casey et al., 2016). There has been considerable research on sea ice classification where C-band SAR is utilized as most of the ice service agencies use C-band SAR (e.g. the European Remote Sensing (ERS)-1/2, RADARSAT-1/2, and Sentinel-1) for operational ice monitoring. Several studies have suggested that L-band SAR can be more useful in sea ice monitoring than the widely used C-band SAR due to the benefits of using longer wavelength signals (Casey et al., 2016; Howell et al., 2018). As radar waves with a longer wavelength can have larger penetration depth into snow on sea ice, using L-band SAR data is more suitable for characterizing sea ice surface structure and type, especially during the melting period (Dierking and Busche, 2006). Different types of sea ice in summer can be distinguishable from one another in the backscattering properties of L-band SAR, which would be difficult in other popularly used frequencies such as C-band, X-band, and Ku-band. However, L-band SAR has been relatively less explored in Cryosphere applications than other bands. Considering upcoming satellites such as the Comisión Nacional de Actividades Espaciales (CONAE) SAtélite Argentino de Observación COn Microondas (SAOCOM) satellite series equipped with L-band SAR, the National Aeronautics and Space Administration (NASA) - Indian Space Research Organization (ISRO) Synthetic Aperture Radar (NI-SAR), and the Japan Aerospace Exploration Agency (JAXA) Advanced Land Observing Satellite-4 Phased-Array L-band Synthetic Aperture Radar-3 (ALOS-4 PALSAR-3), more research on L-band SAR in Cryosphere applications is necessary.

Mahoney et al. (2004, 2014) used vector gradient differences generated from three consecutive SAR images to detect fast ice edges along the Alaskan Arctic coast. The method was successfully applied in the mid-winter season, but manual examination was needed for the other seasons. Li et al. (2018) recently improved the vector gradient difference method by including a median edge detection method over East Antarctica, but it still has a limitation as they used a landfast ice edge as reference data for the nine-year study period. Image correlation analysis based on a feature-tracking algorithm was conducted by Giles et al. (2008) for detection of fast ice regions in East Antarctica using RADARSAT ScanSAR images in 1997 and 1999, even if fast ice changes on shorter timescales (e.g., 5 days) remain as an unresolved issue. Fast ice variability on shorter timescales needs to be explored as the occasional breakouts of fast ice are closely connected with polynyas and ice sheet (Giles et al., 2008). Karvonen (2018) used a temporal cross-correlation method with dual-polarized Sentinel-1 SAR images of a two-week period to detect Arctic fast ice regions. Most recently, Interferometric SAR (InSAR) approaches have been applied to distinguish fast ice regions (Meyer et al., 2011; Han et al., 2015; Dammann et al., 2016, 2019). As recent satellite SAR images have a short repeat cycle (e.g., 6- to 12-day repeat cycle for Sentinel-1), it shows less difficulty in detecting fast ice using InSAR with a small loss of interferometric coherence (Dammann et al., 2019). However, InSAR and offset tracking methods can only use images obtained in accordance with the repeat cycle in the same orbit. This study is focused on detecting fast ice using images taken at different satellite positions with a 5-day interval. We used SAR images with a baseline of 5 days that are not in the same orbit but overlap each other, which is possible because observation areas of adjacent orbits are overlapped a lot in the polar regions. Then, it would be able to classify sea ice at a high temporal resolution than using images with a repeat cycle in the same orbit.

In this paper, we propose a new method that combines image segmentation, image correlation analysis, and machine learning techniques for detecting fast ice regions over West Antarctica. Specifically,

this study develops an algorithm for object-based fast ice detection that adopts object correlation image analysis using bi-temporal L-band SAR images with a short temporal separation (5-days). There are no studies that require the use of specific time period over which fast ice remains stationary (Mahoney et al., 2006). The present study defines fast ice as ice that is in little movement for 5 days and attached along the coast. Previous studies have used a time period of from 3 to 20 days to determine what constitutes fast ice (Barry et al., 1979; Mahoney et al., 2006; Fraser et al., 2010). Object-based classification has the potential to achieve accurate feature extraction since pixel-based classification might be inappropriate with SAR images of high spatial resolution due to the difficulty of interpretation resulting from speckle noise and high spatial heterogeneity (Karvonen, 2004; Casey et al., 2016). As fast ice regions are recognized as being spatially continuous with little change of movement, object-based analysis is desirable for the detection of fast ice areas. After applying image segmentation to SAR composite images, object correlation image analysis was conducted based on the characteristics of motionless and stationary fast ice regions, which result in highly correlated fast ice regions over time. Machine learning techniques including random forest (RF), extremely randomized trees (ERT), and logistic regression (LR) were applied to the segmented fast ice image pairs to develop fast ice classification models. The trained models were applied to various fast ice regions in ocean sectors of West Antarctica to demonstrate the applicability of the proposed approach.

2. Data and methods

2.1. Process description and study area

The data processing flow of the proposed approach in this study is illustrated in Fig. 1. First of all, SAR images, used as main data, are preprocessed and then composited with a pair of images (Section 2.2), then image segmentation is performed for the preprocessed composite images (Section 2.3). For each object of segmented images, input variables for fast ice and pack ice regions are extracted including statistical and contextual variables (i.e., object correlation images). To construct fast ice and pack ice reference data, time series of SAR images in a certain time interval (5-days) are used (Section 2.4). The

Fig. 1. Data process flow chart of the approach in this study.

constructed datasets are applied to machine learning approaches to develop fast ice classification models (Section 2.5). SAR images with fast ice regions from four ocean sectors including Weddell Sea, Bellingshausen Sea, Amundsen Sea, and Ross Sea in West Antarctica form the study regions (Fig. 2). From each ocean sector, training and validation datasets were extracted to construct fast ice classification models and a separate test dataset to evaluate the models.

2.2. ALOS PALSAR data

Level 1.5 geo-referenced images from the Advanced Land Observing Satellite Phased Array L-band SAR (ALOS PALSAR) were used as main data for the detection of fast ice in this study. PALSAR is an active microwave sensor using L-band with a center frequency of 1.27 GHz. PALSAR images are distributed free of charge by the Alaska Satellite Facility (ASF) to public users. Table 1 shows the detailed information of SAR image pairs selected for this study including the names of each site, dates of images, incidence angle at scene center determined by sensor platform orientation, Earth's geometry, and electronic boresight, and usage. All the SAR images are wide-swath ScanSAR mode data consisting of 5 sub-swaths with a swath width of 350 km, horizontal-horizontal (HH) polarization, descending flight pass direction, and the range and azimuth pixel size of 100 m with a time interval of 5 days. ALOS PALSAR L-band HH images were used due to data availability. Although ALOS PALSAR orbit has a revisit time of 46 days, pairs of images in a short time interval can be obtained for areas where fast ice regions overlap in polar regions. This approach is intended to obtain images with high temporal resolution even from polar orbiting satellite sensors with long repetition cycles. We can thus have the benefit of interpreting short-term fast ice deformation events occurring on a time scale of several days.

The ALOS PALSAR ScanSAR mode has a wide range of incidence angles of 18–43°. Incidence angle correction is needed when backscattering coefficients can change in the same sea ice type as the incidence angle changes (Zakhvatkina et al., 2013; Lang et al., 2016). However, in this study, incidence angle normalization was not performed for several reasons. Incidence angle correction generally requires accurate reference data for all sea ice types over study regions (Zakhvatkina et al., 2013). Mahmud et al. (2018) proposed a method using a mean incidence angle dependency for each first-year ice (FYI) and multiyear ice (MYI) over the Arctic in winter for incidence angle correction. They used the Canadian Ice Service Digital Archive (CISDA) regional ice charts to correct incidence angle by sea ice type. In this study, we examined the ice charts from the National Ice Center (NIC; https://www.natice.noaa.gov/). The ice charts are produced mainly with various satellite images with different spatial resolutions ranging from coarse (e.g., Special Sensor Microwave Imager (SSM/I)) to finer scales (e.g., RADARSAT and Advanced Very High Resolution Radiometer (AVHRR)). Therefore, the spatial resolution of the NIC ice charts can range approximately from 10 m to 50 km. According to the NIC weekly/bi-weekly ice analysis products (i.e., sea ice chart) available for the study regions, a majority of the regions were just classified as "Undetermined/Unknown" or "Old Ice" that can be FYI, second-year ice, or MYI according to the WMO sea ice nomenclature. Accurate incidence angle correction would not be guaranteed without detailed and accurate information about sea ice types for the study regions. Komarov and Buehner (2019) recently found that incidence angle correction does not always contribute to the increase in accuracy of sea ice classification. In addition, the L-band SAR is relatively less sensitive to small changes in sea ice surface (Dierking and Busche, 2006; Meyer et al., 2011; Dammann et al., 2016). We suppose that as SAR image pairs used in this study have incidence angle differences of less than 3°, changes in backscattering for each sea ice type would not be significant. In this study, the capability of the proposed approach for fast ice detection over West Antarctica is demonstrated in a variety of regions and dates, without incidence angle correction and post-processing (more in the
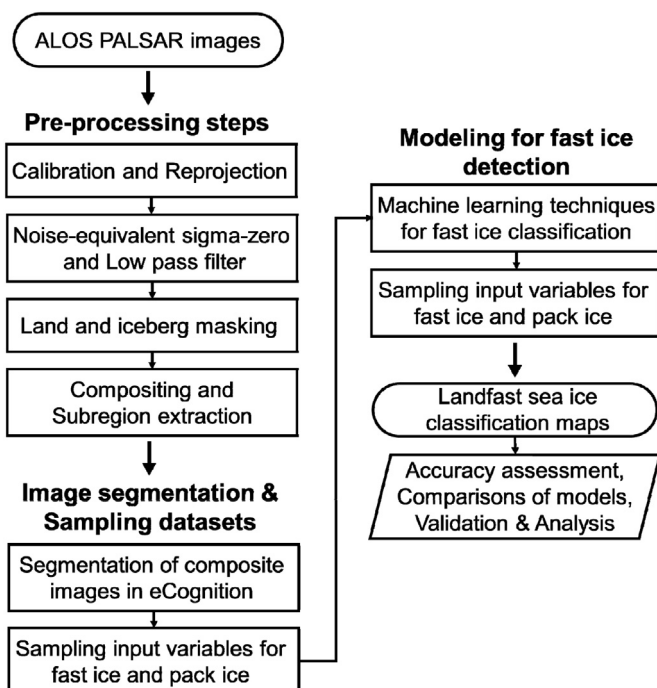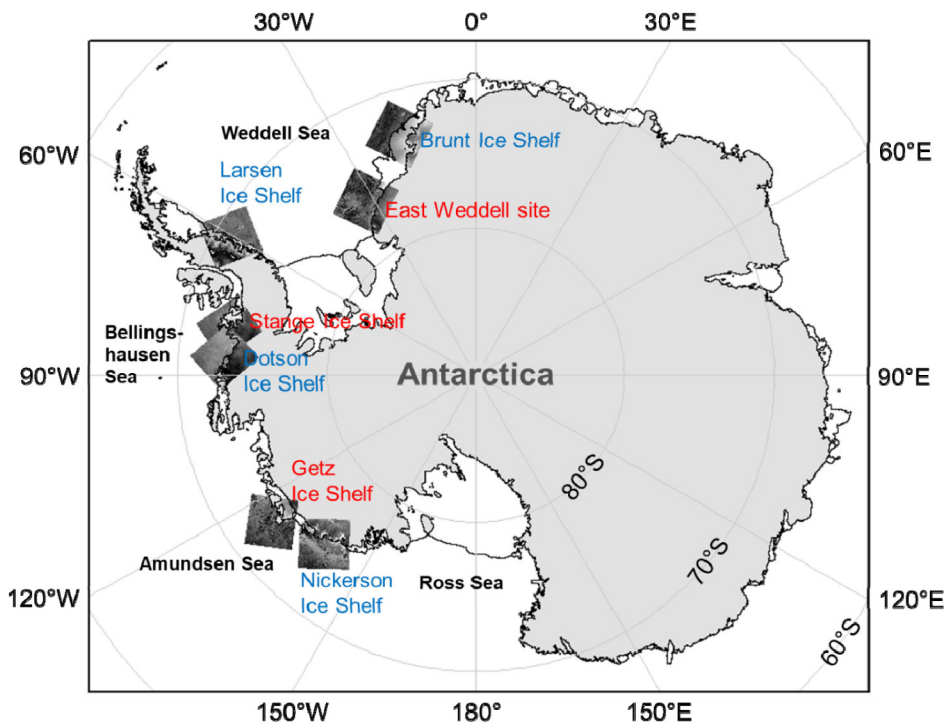
Fig. 2. Map of study area including landfast sea ice regions over West Antarctica with ALOS PALSAR images over the Weddell Sea, Bellingshausen Sea, Amundsen Seas, and Ross Sea sectors. Regions (red letters) in Weddell Sea were used for constructing training and validation datasets and the other regions (blue letters) for test dataset. (For interpretation of the references to color in this figure legend, the reader is referred to the web version of this article.)

Table 1
The information of ALOS PALSAR image pairs. All the image pairs are separated by 5 days.

Sector	Site	Date (for a pair of images)	Scene Center Incidence angle	Usage
Weddell Sea	East Weddell	8 Aug. 2007	34.112°	Training and validation
		13 Aug. 2007	34.107°	
	Brunt Ice Shelf	8 Aug. 2007	34.078°	Test
		13 Aug. 2007	34.090°	
	Larsen Ice Shelf	20 Aug. 2007	34.106°	Test
		25 Aug. 2007	34.086°	
Bellingshausen Sea	Stange Ice Shelf	7 Oct. 2010	34.099°	Training and validation
		12 Oct. 2010	34.101°	
	Dotson Ice Shelf	13 Nov. 2010	34.103	Test
		18 Nov. 2010	34.103	
Amundsen Sea	Getz Ice Shelf	31 Oct. 2010	34.091°	Training and validation
		5 Nov. 2010	34.092°	
	Nickerson Ice Shelf	26 Jul. 2007	34.095°	Test
		31 Jul. 2007	33.979°	

discussion section).

Training, validation, and test datasets were extracted from each of the ocean sectors, the usage of which is explained in Section 2.5. A total of 7 image pairs were selected over 1) Weddell Sea sector including East Weddell, Brunt Ice Shelf, and Larsen Ice Shelf, 2) Bellingshausen Sea sector including Stange Ice Shelf and Dotson Ice Shelf, and 3) Amundsen Sea sector including Getz Ice Shelf and Nickerson Ice Shelf. The image data were collected between July and August 2007 and again between October and November 2010. Level 1.5 SAR images are multi-look processed and georeferenced images with general radiometric and geometric calibration (Lee et al., 2015). The selected images were preprocessed in the MapReady software (version 3.1.24) developed by the Alaska Satellite Facility (ASF). First, the amplitude in SAR images was converted into a radiometrically calibrated power image in order to use SAR data in a quantitative manner. The SAR images with backscatter values were calibrated into sigma-0 (nought) in power scale, which intends to use the calibrated values that refer to the ground. Then, the values were scaled into decibel (dB) values by applying a logarithmic function ($10 \cdot \log_{10}$(calibrated values)). SAR geometry was transformed into polar stereographic map projection with a bilinear resampling method and a specified pixel size of 100 m. The noise-equivalent sigma-zero (NESZ) was -25 dB, below which pixel values were discarded. A low pass filter of a 5×5 pixel window was applied to the preprocessed images to reduce speckle. After preprocessing, each image within an image pair was masked for the overlaid regions and then composited for image segmentation (Section 2.2). Fast ice regions that might not be readily visible in a single image can be revealed from the composite of bi-temporal images. As the composite of two images enables the detection of spatiotemporal changes between the two, fast ice regions can be captured in the composite image with the pixel values that remain relatively constant over time. Composite images were generated using ArcGIS 10.4.1 software. SAR image pairs used in this study have a 5-day interval, as the time scale resulted in the largest number of image pairs available. In addition, a relatively short time period such as 5 days could be useful for detection of rapidly changing fast ice regions.

2.3. Image segmentation and explanatory variables

This study proposes object-based fast ice classification models based

on image segmentation. Image segmentation was implemented in eCognition software (Version 8.7.2; Developer, 2012) on the composite SAR images. Image segmentation is suitable for SAR data with high spatial heterogeneity. This is because classification problems caused by local outliers and noise can be mitigated by grouping pixels with similar characteristics. The multiresolution segmentation algorithm in eCognition was used, which is a bottom-up segmentation method that minimizes the heterogeneity of image objects and maximizes homogeneity to obtain the best segmentation results (Amani et al., 2017; Johansen et al., 2018; Liu et al., 2018). The segmentation process is conducted based on several user-defined criteria with three parameters (i.e., scale, shape, and compactness; Belgiu and Drăguţ, 2014). For more detailed explanation about the segmentation process, please refer to Appendix A. In this study, various combinations of weights for the scale, shape, and compactness parameter fields were tested, and an optimized combination was determined based on visual inspection of resulting objects.

A total of 5 input variables—contextual variables of object correlation images (OCI) analysis (i.e., Correlation, Slope, and Intercept) and statistical variables such as Mean and standard deviation (STD)—were extracted from objects of the segmented composite images (Table 2). Over a five-day period, it would be feasible to evaluate the horizontal movement of sea ice to detect if it is fast or pack ice. Based on the bi-temporal imagery, those input variables can show differences in back-scatter (i.e., evidence for motion) to distinguish ice types (i.e., fast and pack ice). The contextual variables were calculated with pixels within each object of the composite images. The magnitude and direction of changes of spectral pixel values in an object of the composite images are used for the OCI analysis (Im and Jensen, 2005; Im et al., 2008). If there is little or no change between the two dates of images (i.e., fast ice), correlation coefficients of pixel values from two dates should be high. Otherwise, correlation coefficients are generally low or intermediate when changes significantly or moderately occur (i.e., pack ice). The other information in the OCI analysis are slope and intercept, which can be useful in detecting changes when correlation coefficients are high. The correlation (X), slope (slp), and intercept (Z) images are computed as the following Eqs. (1)–(3), respectively (Im et al., 2008).

$$X = \frac{N \times B \times \sum_{i=1}^{B} ZD1D2_i - (\sum_{i=1}^{B} ZD1_i \times \sum_{i=1}^{B} ZD2_i)}{\sqrt{(N \times B \times \sum_{i=1}^{B} ZD1D1_i - (\sum_{i=1}^{B} ZD1_i)^2) \times (N \times B \times \sum_{i=1}^{B} ZD2D2_i - (\sum_{i=1}^{B} ZD2_i)^2)}}$$
(1)

$$slp = \frac{N \times B \times \sum_{i=1}^{B} ZD1D2_i - (\sum_{i=1}^{B} ZD1_i \times \sum_{i=1}^{B} ZD2_i)}{N \times B \times \sum_{i=1}^{B} ZD1D1_i - (\sum_{i=1}^{B} ZD1_i)^2}$$
(2)

$$Z = \frac{\sum_{i=1}^{B} ZD2_i - slp \times \sum_{i=1}^{B} ZD1_i}{N \times B}$$
(3)

where N is the image with the number of pixels for each object from the image segmentation, B is the number of input bands, which is 2 (i.e., temporally separated images of two dates) in this study, $ZD1_i$ and $ZD2_i$ are the images from date 1 and 2 for each channel i zonally summed

Table 2
Information of the input variables used to develop fast ice detection models in this study.

Type	Input features
Contextual variables	Correlation
	Slope
	Intercept
Statistical variables	Mean of composite imagery including layer 1 (earlier date) and 2 (later date)
	Standard deviation (STD) of composite imagery

based on the objects, $ZD1D1_i$, $ZD1D2_i$, and $ZD2D2_i$ are the images multiplied by each date by itself and date 1 and 2 for each channel i and zonally summed based on the objects, and Slp indicates the slope image obtained by the Eq. 2.

The Mean variable could be helpful in discriminating fast ice from pack ice regions. The segmented objects over fast ice regions consist of relatively homogeneous fast ice areas. Meanwhile, pack ice regions can have a more complex texture depending on the ratio of ice floes, open water, and open water covered with very thin ice. The STD variable could also be an important indicator. Changes in spectral values over fast ice regions between two images with a 5-day interval are generally small when compared to pack ice with relatively larger changes in backscatter coefficients over time. In addition, we tested some combinations of input variables through the machine learning methods used in this study with a statistical hypothesis test (not shown). According to the preliminary results, there was no significant difference in models, except for a model that used only the correlation variable and showed a significant decrease in accuracy. Although slope and intercept were highly correlated, they could convey different information that helps to detect changes (Im and Jensen, 2005; Im et al., 2008). Therefore, we decided to use all input variables that resulted in the highest accuracy.

2.4. Construction of reference for fast ice and pack ice

Reference regions for fast ice and pack ice were determined based on visual interpretation of the preprocessed SAR composite images in a 5-day time interval. Seaward fast ice edges were determined by discriminating fast ice and pack ice regions by analyzing the characteristics of surrounding features and the backscatter evolution (shown as red solid lines in Fig. 3). Fast ice is found adjacent to ice shelves and also in-between grounded icebergs (Massom et al., 2001; Giles et al., 2008; Fraser et al., 2012). Icebergs were masked out using a set backscatter threshold. In this study, this threshold was empirically determined to be −11 dB. Icebergs generally show higher backscatter than their surroundings which often is a mixture of open water and sea ice (Williams et al., 1999; Mazur et al., 2017). In particular, icebergs can be visually discriminated against level fast ice they embedded, while they may not always show a distinct contrast within heavily deformed sea ice (Wesche and Dierking, 2012; Wesche and Dierking, 2015). Fast ice regions show temporally consistent backscattering compared to pack ice regions as shown in Fig. 3. The fast ice edge is identified by a line of consistent backscatter. To assess the validity of visual interpretation-based reference regions, time series of MODIS optical images with 250 m resolution (MOD02QKM product, which is Level 1B calibrated radiances data) were used (Massom et al., 2010; Kim et al., 2015). Fig. 4 shows that SAR and MODIS images available in a 5-day time interval (31 Oct. 2010–5 Nov. 2010) for fast ice near the Getz Ice Shelf to qualitatively validate the presence of fast ice. As delineated by the outermost edge (red line) to traverse between the fast ice and background area, fast ice areas in the MODIS images are recognizable. Finally, a total of 1068 samples (i.e., objects) used for training and validation were constructed from the reference fast and pack ice regions generated from SAR images. All samples were randomly divided into 80% for training set to develop machine learning-based fast ice classification models, and 20% for validation set to evaluate their performances. We assessed the performance of the three trained models with test dataset that are not included in the training and validation data.

2.5. Machine learning techniques for fast ice classification

The machine learning approaches used in this study are random forest (RF), extremely randomized trees (ERT), and logistic regression (LR) for developing fast ice classification models using the training and validation datasets. They have been widely used in the field of remote sensing to solve various classification and regression problems (Yoo
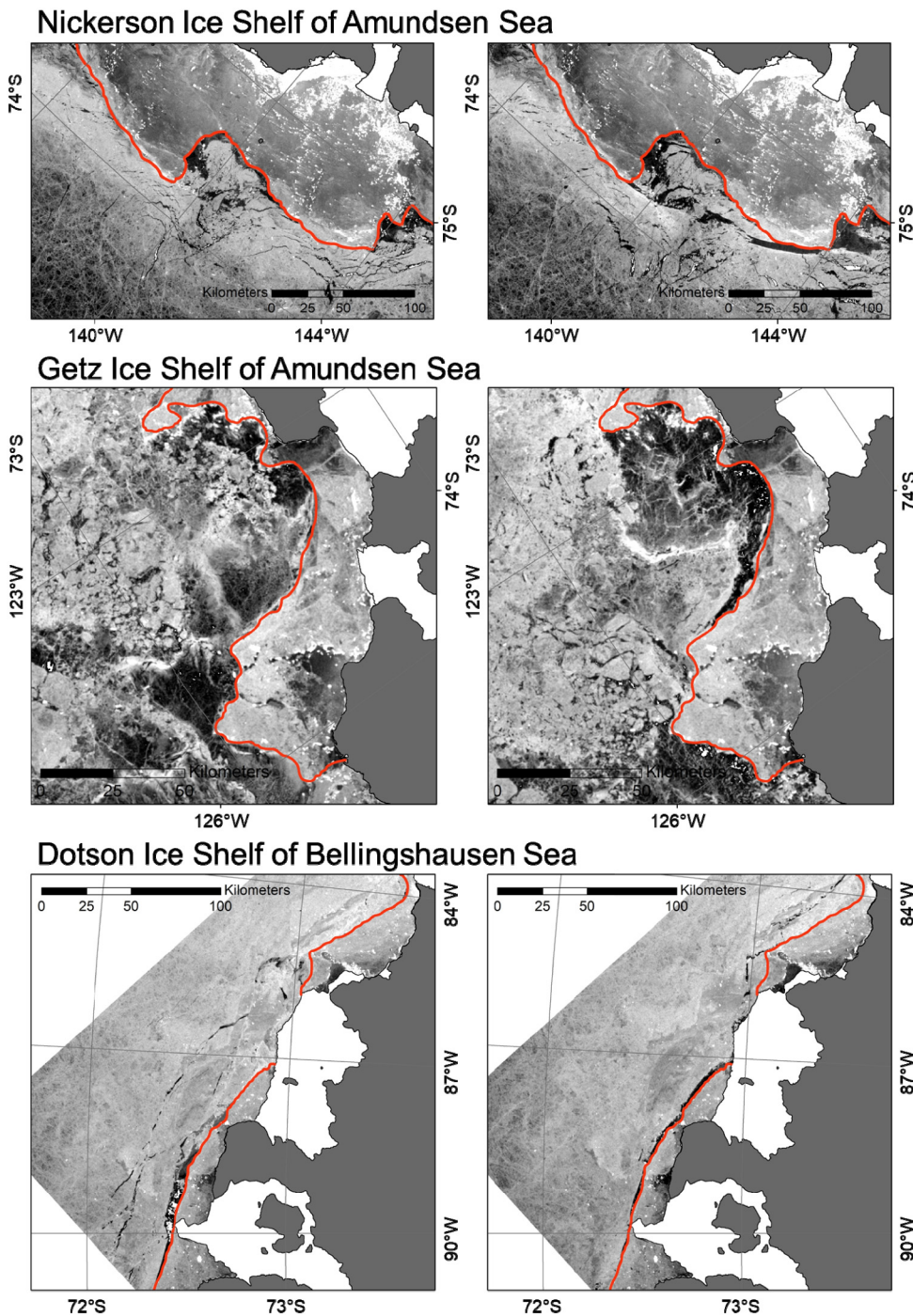
Nickerson Ice Shelf of Amundsen Sea

Getz Ice Shelf of Amundsen Sea

Dotson Ice Shelf of Bellingshausen Sea

Fig. 3. Example of backscatter image of L-band HH-pol ALOS PALSAR SAR separated by a 5-day time gap used to detect fast ice edge for reference over Amundsen Sea and Bellingshausen Sea sectors (refer to Table 1 for the detailed description of image pairs). The Antarctic continent and ice shelves are shown as solid dark gray and white areas, respectively. The text in italic shows fast ice and pack ice regions. Red solid lines indicate the reference fast ice edge delineated by visual interpretation of the two images with a 5-day time interval. (For interpretation of the references to color in this figure legend, the reader is referred to the web version of this article.)

et al., 2012; Barrett et al., 2014; Lee et al., 2017; Richardson et al., 2017; Mutowo et al., 2019; McLaren et al., 2019). RF is a collection (i.e., ensemble) of decision trees using a bootstrap aggregating (Bagging) method (Breiman, 2001). It constructs independent trees with random sampling and combines final results from the trees using an ensemble method such as voting or weighted voting for classification (Sonobe et al., 2017; Wylie et al., 2019). RF was implemented in R software with an add-on package of random forest (Liaw and Wiener, 2002; Kim et al., 2017). In this study, options used for constructing a random forest model in R were set as default for the number of trees (500) and variables sampled at each node (generally n where n is the number of input variables) and the minimum size of terminal nodes. It also provides relative variable importance as Mean Decrease Accuracy (MDA) (Rhee and Im, 2017). MDA is calculated using out-of-bag (OOB)

data, which is left out of the training data in each tree. Misclassification rates are calculated using OOB data and a variable-permuted OOB data using a given tree, which is repeated for all trees. MDA means the average increase in the misclassification rate (Jang et al., 2017). The higher the MDA it is, the more important the variable is to classify fast ice and pack ice class.

ERT is a relatively new tree-based ensemble classifier method compared to RF (Geurts et al., 2006). It extends RF by introducing a different randomization to splitting at nodes. While RF finds the best node splitting points among the input variables selected at each node when constructing trees, ERT performs node splitting fully at random and uses the same variable set with no bagging for each tree, further reducing the variance between trees and minimizing the bias. ERT was implemented using the add-on package of "ExtraTrees" in R with
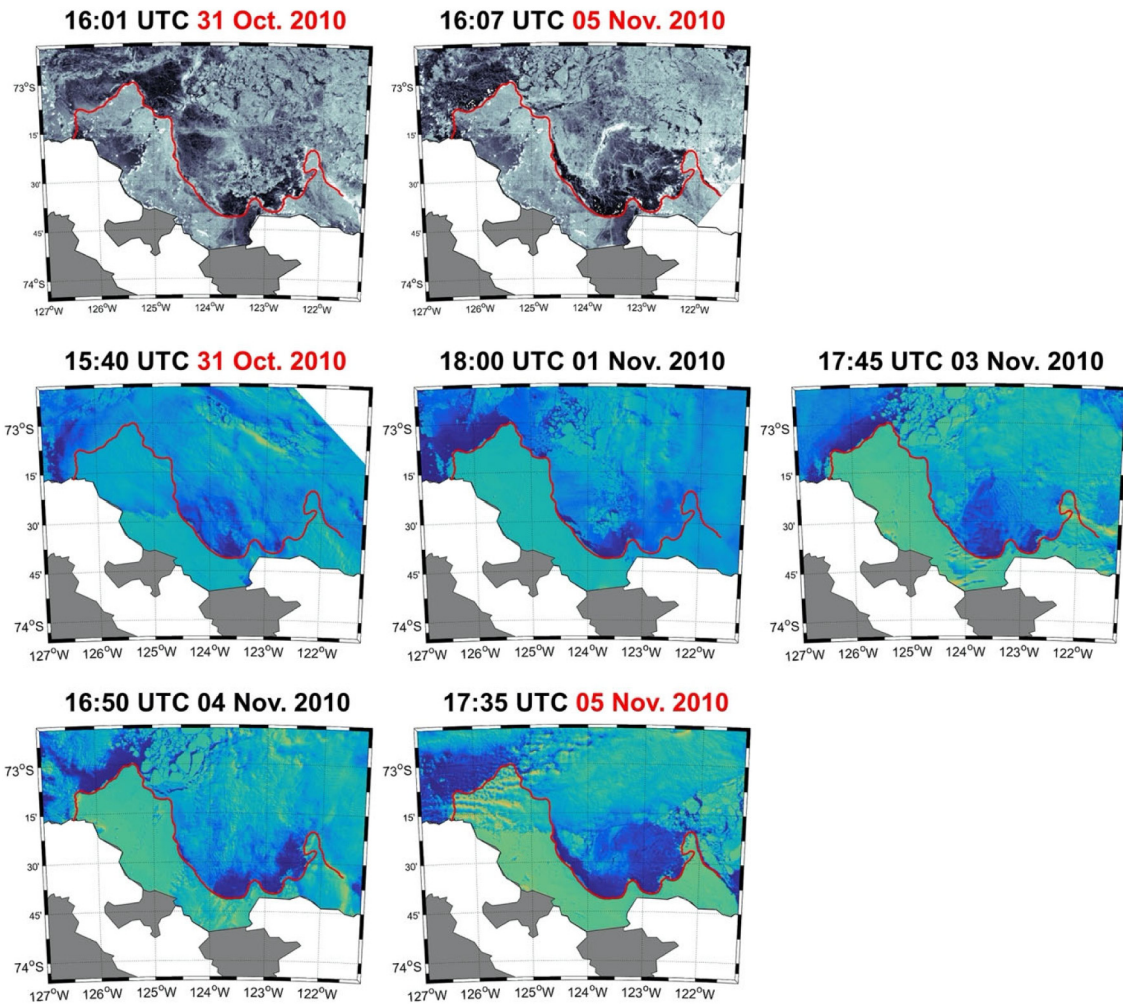
Fig. 4. Maps of fast ice near the Getz Ice Shelf in the Amundsen Sea from two SAR images (top) and MODIS calibrated radiances images available between 31 October 2010 and 5 November 2010 (middle and bottom). Red solid lines indicate the reference fast ice edge delineated by visual interpretation of the two images with a 5-day time interval. (For interpretation of the references to color in this figure legend, the reader is referred to the web version of this article.)

default parameters.

LR is a regression model applicable to categorical variables to estimate the probability of an event occurrence (i.e. the probability of being classified as fast ice). Similar to a linear regression model, it models the relationship between independent variables and dependent variables with a specific function (Lee et al., 2017). LR is used for classification as output ranging from 0 (non-fast ice) to 1 (fast ice) that is divided by a fixed threshold by using a logistic (sigmoid) function (4).

$$\text{Prob}(Y \mid X_1, X_2, ..., X_n) = \frac{1}{1 + \exp[\sum_{i=1}^{n} w_i x_i]} \quad (4)$$

where $\text{Prob}(Y|X_1,X_2, ...,X_n)$ is the probability of the dependent variable Y (i.e., fast ice and pack ice, target classes) given X_n ($n = 1, 2, ..., n$) (i.e., input variables), n is the number of independent variables, X_i indicates an ith independent variable, and w_i is the coefficient for variable Xi. The logistic function estimates the probability of a class (fast ice or pack ice). The LR implementation with an add-on package called "glm" in R was used. In this study, we used a threshold of 0.5 above which objects are assigned as fast ice.

Model performance was evaluated using confusion matrices with producer's and user's accuracy (PA and UA, respectively), overall accuracy (OA), and kappa coefficients. Using RF and LR outputs, we examined which variables were most sensitive to fast ice detection. For model validation, the classification models were applied to fast ice regions in the Weddell Sea, Bellingshausen Sea, Amundsen Sea, and Ross Sea.

3. Results and discussion

3.1. Segmentation parameterization

We tested a total of 60 combinations with different weights in scale parameters of 15, 20, 25, and 30, shape parameters of 0.1, 0.3, 0.5, 0.7, and 0.9, and compactness parameters of 0.1, 0.3, and 0.5. Fig. 5 shows some of segmentation results tested with various combinations of parameters. The optimized parameter combination was determined to be 25, 0.1, and 0.5 for scale, shape, and compactness parameters, respectively. The three parameters were interactively involved in the segmentation results. The overall segmentation quality was basically examined for both over-segmentation and under-segmentation. Over-segmentation was avoided by controlling the level of detail based on an appropriate scale value (Fig. 5a). The scale threshold was adjusted to make visually identified ice objects larger than the size of the segmented objects in order to avoid mixed fast ice objects with pack ice regions. The objects should not be too small to contain sufficient statistical information. As shown in Fig. 5a, the smaller the value of the scale parameter is, the smaller the objects are produced, and vice versa. The scale threshold of 25 was found to achieve reasonable segments with clear boundaries between the fast ice and pack ice regions and the minimal isolated segments (Fig. 5a). With regard to the shape
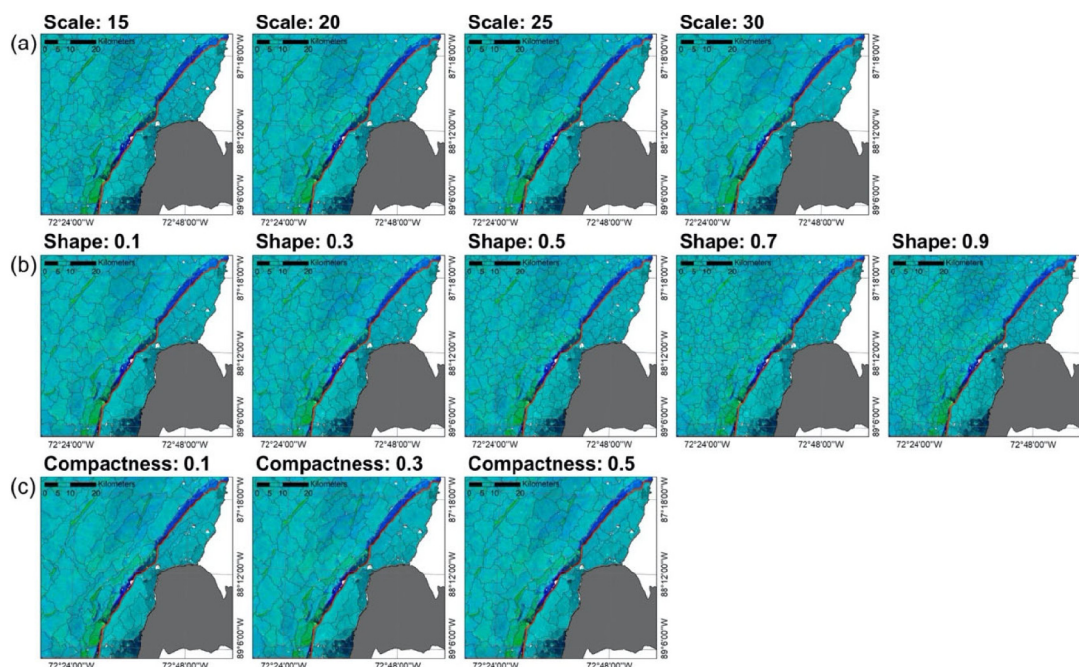
Fig. 5. Examples of segmentation results at different (a) scale parameters with fixed thresholds for shape of 0.1 and compactness of 0.5, (b) shape parameters with scale of 25 and compactness of 0.5, and (c) compactness parameters with scale of 25 and shape of 0.1 parameter setting. The red solid line indicates reference fast ice edge. The background is a false color composite image of date 1 (green) and date 2 (blue) over a part of landfast sea ice region off the Dotson ice shelf, the Bellingshausen Sea sector. (For interpretation of the references to color in this figure legend, the reader is referred to the web version of this article.)

parameter, using a smaller shape value produced better segmentation results with a distinct difference in the backscatter coefficients between objects (Fig. 5b). In more detail, the difference between the shape of 0.1 and 0.9 is clearly seen along the edge of fast ice areas (red sold lines), showing that the segments with the shape of 0.9 are mixed with fast ice and pack ice regions. The objects with the shape of 0.1 better captured patterns on backscattering. Regarding different compactness, it is shown that a more compact and smaller sized objects were produced using a larger compactness parameter (Fig. 5c). Compactly segmented objects will have better statistical estimates for local changes than others, which enables more accurate classification afterwards.

Fast ice regions are particularly noticeable due to the high correlation values in the correlation map (Fig. 6a). This is because the variations in the pixel values over fast ice regions are small, resulting in high correlation when compared to the pack ice in subsequent images. It also indicates that the STD variable is able to distinguish fast ice from pack ice in this regard. The Mean variable image shows a distinct separation in the areas where polynyas occur showing relatively low backscatter (i.e., between fast ice and pack ice and between pack ice and the Antarctic land in Fig. 6d). As a polynya may be covered by very thin ice, the areas can show relatively low backscatter values (Dierking and Busche, 2006; Howell et al., 2018). On the contrary, the situation can be altered by other influences such as wind conditions (Dierking and Busche, 2006; Wesche and Dierking, 2015). Wind-roughened open water can have much higher backscattered signals (Dierking and Busche, 2006). However, in this case, objects over pack ice regions containing open water would have highly variable backscattering values from time series of images, leading to lower correlation or higher STD values when compared to fast ice regions.

3.2. Model evaluation and variable importance

Model evaluation results using the validation set are shown in Tables 4-6. All three models produced similar results. The ERT model produced the best performance with an OA of 97.21% and a kappa coefficient of 0.94, while RF and LR models resulted in slightly lower

performances with an OA of 96.74% and a kappa of 0.93. The fast ice class shows slightly higher PA than the pack ice class in all three models although the sample size of the pack ice class was twice that of the fast ice class. Different sample sizes of the two classes including 1:1, 1:2, and 1:3 for fast versus pack ice class were tested and 1:2 was identified as the most reasonable to classify fast ice regions with minimum commission and omission errors. Meanwhile, UA was lower for fast ice class than pack ice class as some of the pack ice samples were misclassified as fast ice class, which means that fast ice regions might have been slightly over-detected. A slight over-segmentation might account for the over-detection of fast ice because uniform backscattering over time can occur by chance on very small objects far from the coast. A few of small pack ice objects from near the seaward fast ice edge were misclassified as fast ice as well due to the stationary backscatter strength of small segments. Meanwhile, fast ice objects located at the edge of seaward fast ice were occasionally misclassified as pack ice due to low correlation between subsequent images. The stability of fast ice generally decreases toward the edge of fast ice (Dammann et al., 2016). In particular, seaward young and thin fast ice is less stable due to sheer by pack ice. On the one hand, heavy snow load on sea ice often depresses the ice below ocean water level, which then results in a slush layer at the basal snow layer on ice. This is so called a negative freeboard, especially in Antarctica (Massom et al., 1997). The process at the snow-ice interface can also affect the backscatter signatures (Wesche and Dierking, 2012), which can cause classification errors.

Fig. 7 shows the relative variable sensitivity identified by RF and LR models with MDA and p-value transformed to the negative logarithmic scale, respectively. Correlation and STD variables were identified as important variables to discriminate fast ice from pack ice regions in both RF and LR models. Correlation was highly significant since fast ice is an almost motionless feature compared to pack ice over the synoptic timescale (e.g., 5 days used here), which yields high correlation between two dates of imagery in fast ice regions and low correlation in pack ice regions. Secondly, the STD variable was considered to be the second significant variable for both models. This was because short-term backscatter variations in objects are larger for pack ice than for
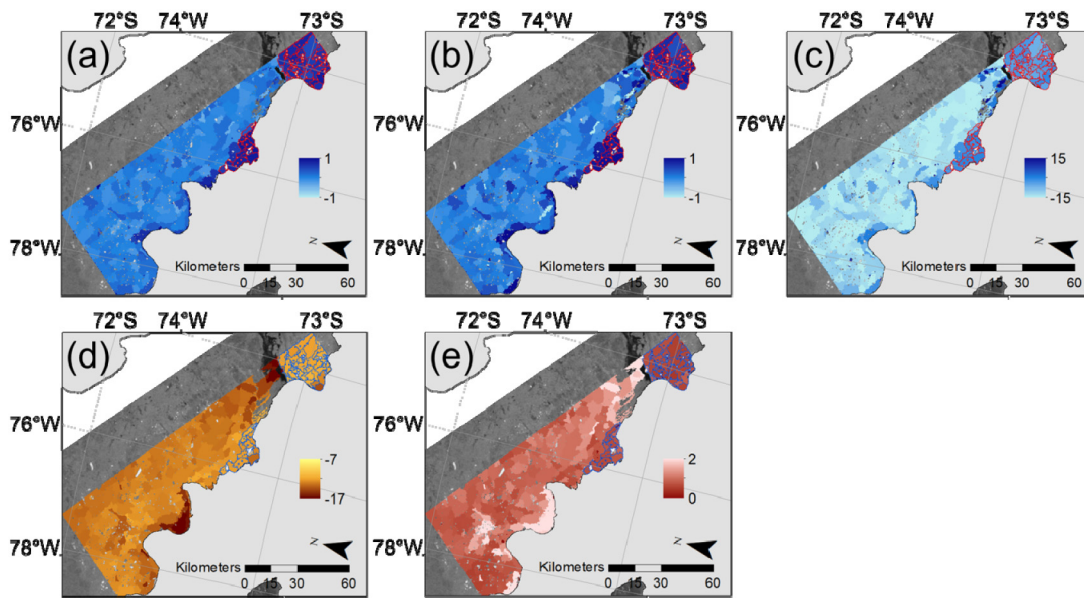
Fig. 6. Input variables extracted based on the segmentation result including (a) Correlation, (b) Slope, (c) Intercept, (d) Mean of backscatter coefficient (in dB) for combined dates 1 and 2, (e) Standard deviation of backscatter coefficient for combined dates 1 and 2. The background image is the ALOS PALSAR SAR image for the landfast sea ice region off the Stange ice shelf, the Bellingshausen Sea sector. Gray area in the lower right is the Antarctic land, and red and blue solid lines over sea ice zone indicate the reference fast ice edge. (For interpretation of the references to colour in this figure legend, the reader is referred to the web version of this article.)

Table 4
Accuracy assessment result of the random forest model for the validation set. The entries in the confusion matrix are the number of segments for each class.

Classified as	Reference			
	Fast ice	Pack ice	Sum	User's accuracy
Fast ice	70	5	75	93.33%
Pack ice	2	138	140	98.57%
Sum	72	143	215	
Producer's accuracy	97.22%	96.50%		
Overall accuracy	96.74%			
Kappa coefficient	0.93			

Table 5
Accuracy assessment result of the extremely randomized trees model for the validation set. The entries in the confusion matrix are the number of segments for each class.

Classified as	Reference			
	Fast ice	Pack ice	Sum	User's accuracy
Fast ice	70	4	74	94.59%
Pack ice	2	139	141	98.58%
Sum	72	143	215	
Producer's accuracy	97.22%	97.20%		
Overall accuracy	97.21%			
Kappa coefficient	0.94			

fast ice.

3.3. Performance evaluation of landfast sea ice detection maps

Fast ice detection models were tested for various fast ice regions over the other ocean sectors (Figs. 8–13). To assess the performance and extendibility of the models, test sites which are not included in training were selected in different ocean sites with various conditions considering surrounding pack ice drift, wind exposure, atmospheric temperature, and icebergs that can affect the development and stability of

Table 6
Accuracy assessment result of the logistic regression model for the validation set. The entries in the confusion matrix are the number of segments for each class.

Classified as	Reference			
	Fast ice	Pack ice	Sum	User's accuracy
Fast ice	70	5	75	93.33%
Pack ice	2	138	140	98.57%
Sum	72	143	215	
Producer's accuracy	97.22%	96.50%		
Overall accuracy	96.74%			
Kappa coefficient	0.93			

fast ice. Fig. 8 shows the overall quantitative evaluation results for the models over each study area. All models resulted in very similar accuracies, while the LR model produced the best performance with averaged 82.04% of PA (fast ice), 98.73% of PA (pack ice), 96.93% of UA (fast ice), 92.69% of UA (pack ice), 93.45% of OA, and 0.84 of Kappa. Fast ice edges were extracted as reference data by visual interpretation of the ALOS PALSAR SAR bi-temporal images with a 5-day interval (red solid lines) (Figs. 9–12). Regarding the fast ice objects that were incorrectly classified as pack ice at the edge of fast ice (Figs. 9 and 10), heavy snow load on the ice could be a reason as explained in Section 3.2. As snow loading induces flooding at the snow-ice interface (Massom et al., 1997), the condition can change the backscattering signals and further affect segmentation and classification results. In Figs. 9b and 10c, a few pack ice objects were misclassified as fast ice by the ERT and LR models. As explained in Section 3.2, the misclassifications occurred because a few relatively small objects have high correlation between the two subsequent SAR images due to highly compacted pack ice with limited motion in a short period of time. Unlike the other fast ice regions with relatively high accuracies, the fast ice region off the Larsen ice shelf, Antarctic Peninsula resulted in low PA for fast ice (Fig. 8c). High backscatter over the fast ice region near the Hearst Island of the Larsen D ice shelf (Fig. 11 and Fig. B1 of Appendix B) caused confusion in distinguishing fast ice from ice shelves, causing misclassifications. The fast ice in the region seems to be very
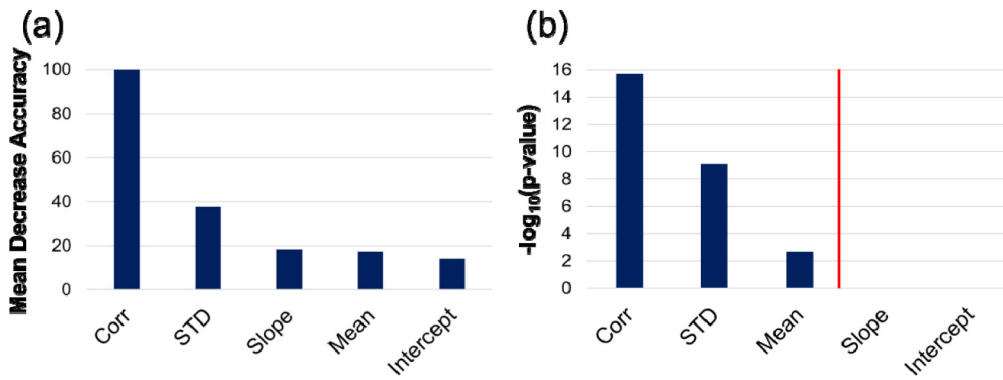
old multi-year sea ice, producing high backscatter as it has aged and thickened changing its properties such as salinity and brine volume. The fractures over fast ice give a further evidence of being fixed to the nearby glacier for decades. Massom et al. (2010) showed a mechanical coupling between multi-year fast ice (MYFI) and the Mertz Glacier Tongue, where rifts from the glacier propagated into the MYFI and contributed to its breakup. As shown in Fig. B1 of Appendix B, many icebergs are trapped in fast ice areas as well. Cook and Vaughan (2010) also reported semi-permanent fast ice formed along the entire Larsen D Ice Shelf, which were difficult to distinguish from the ice shelf front.

Fig. 12 shows that some objects over fast ice areas were incorrectly classified as pack ice over the fast ice regions off the Nickerson ice shelf. The objects have a low probability of fast ice in the LR model as well. Three possible reasons for the misclassification are discussed in the following two paragraphs; these are the effect of snow packs on L-band images, the effect of ice deformation, and the effect of incidence angles (Wolfgang Dierking, personal communication, 2019). A reason for the misclassifications may be due to L-band response to snow packs. Behind the icebergs (bright backscattering spots), there are strips with snow accumulation in the wind shadow (Fig. 12d). This implies that L-band is also influenced by snow packs to a certain degree, even though it has been known that L-band is not sensitive to snow cover as its wavelength is significantly larger than snow grain size (Dammann et al., 2016).

Therefore, the changes in backscattering on the red elliptical circles in Fig. 12d where misclassifications occurred might have been affected by snow as well. Furthermore, the 10-m wind speed over the regions was about 9 m/s according to the European Center for Medium-Range Weather Forecasts reanalysis 5 (ECMWF ERA-5) data of the Climate Reanalyzer (https://climatereanalyzer.org/). Even low wind speed could be strong enough to change the snow structure. Meanwhile, if the temperatures are close to 0 °C, there may also be some changes at the snow-ice interface in terms of roughness, salinity, and moisture, which also change the backscattering (Wesche and Dierking, 2012). However, daily average 2-m maximum air temperature over the regions was approximately -20 °C on 26th July 2007 and -30 °C on 31th July 2007 (5 days later) according to the weather map on $0.5° \times 0.5°$ rectilinear grids of the Climate Reanalyzer, which is generated from the NCEP Climate Forecast System version 2 (CFSV2) and CFS Reanalysis (CFSR) model. It confirms that the fast ice regions were in a dry ice condition as it was in the austral winter season (i.e., July in Antarctica). On the other hand, it may also be possible that the large darker zone in the lower middle of the images is a thinner ice which has been slightly deformed in some places between both data acquisitions. Above the lower red elliptical circle in Fig. 12d, there is a brighter floe (blue rectangular box in Fig. 12d). The darker strips through this floe and around it have almost vanished in the image on 31 July, which may indicate either ice
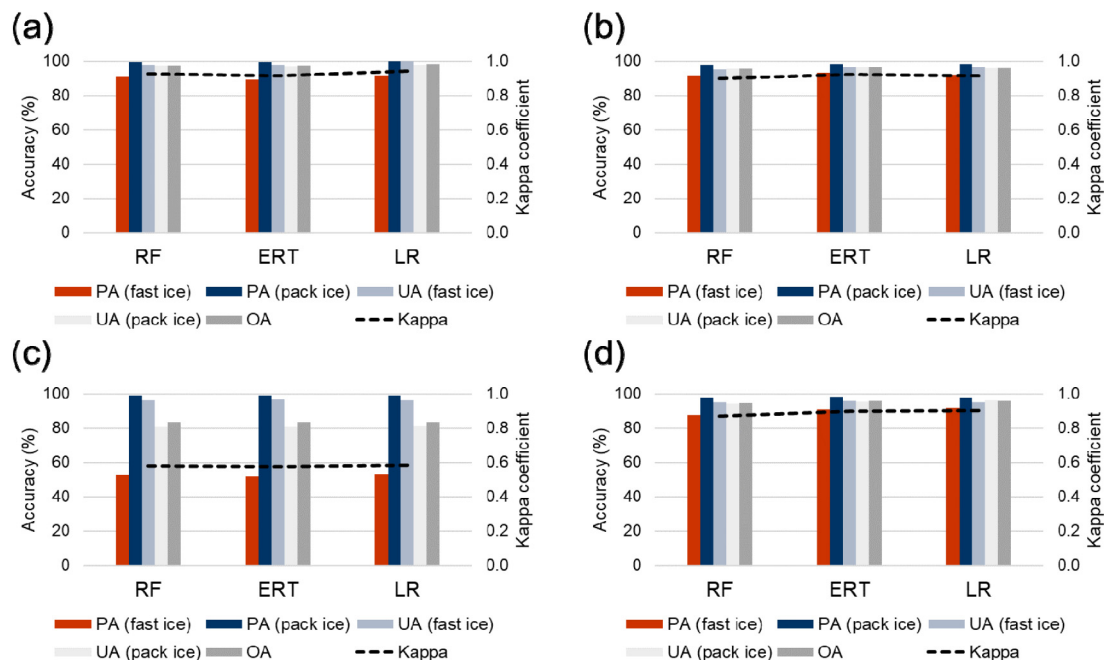

Fig. 8. Performance evaluation of the trained models for landfast sea ice over (a) the Dotson ice shelf, the Bellingshausen Sea, (b) the Brunt ice shelf, eastern Weddell Sea, (c) the Larsen ice shelf, Antarctic Peninsula, and (d) the Nickerson ice shelf, eastern Ross Sea.
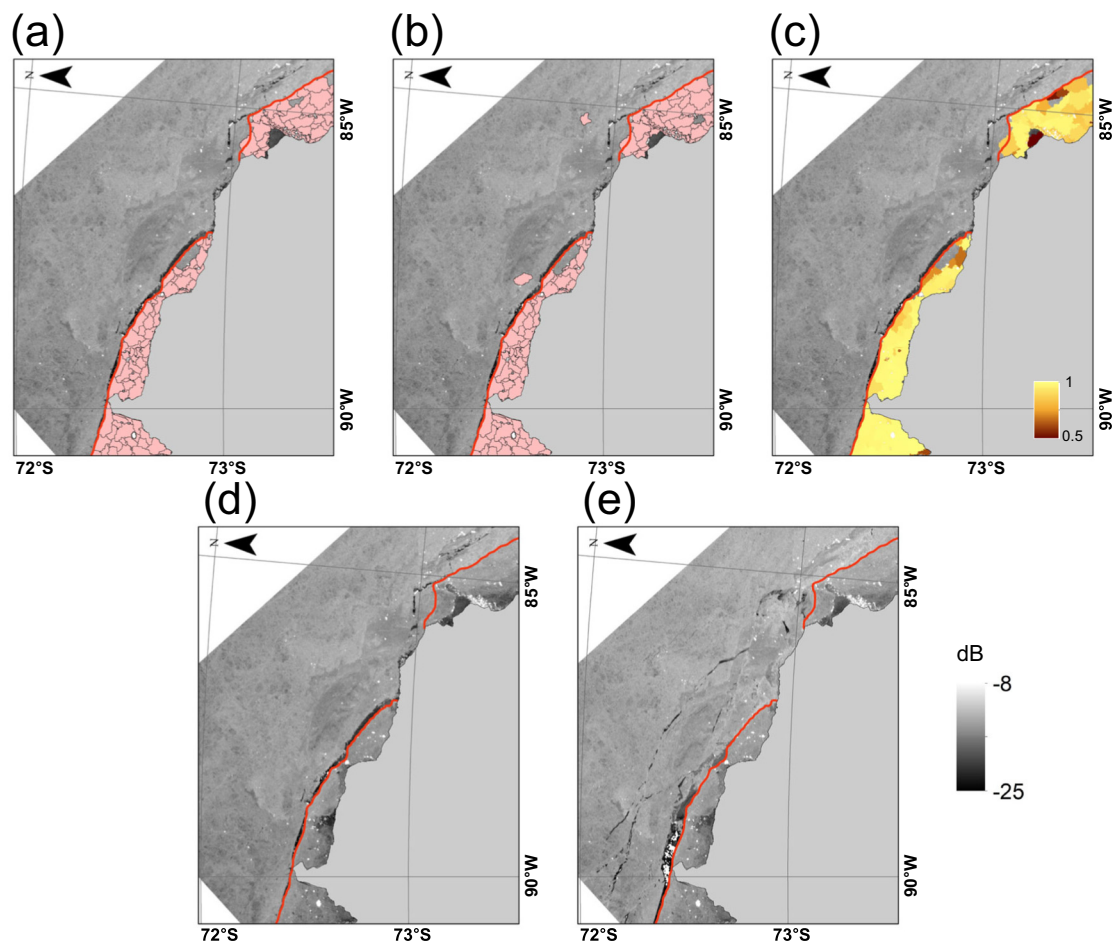
Fig. 9. Landfast sea ice detection results off the Dotson ice shelf, the Bellingshausen Sea of (a) random forest (RF), (b) extremely randomized trees (ERT), (c) logistic regression (LR) models, (d) backscatter image of L-band HH-pol ALOS PALSAR for date 1 (13 Nov. 2010), and (e) backscatter image for date 2 (18 Nov. 2010). Red solid lines indicate the reference fast ice edge, RF and ERT results are shown in pink color and LR result for the probability of fast ice coverage in yellowish-starched color, and gray areas are both Antarctic continent and ice shelves. (For interpretation of the references to color in this figure legend, the reader is referred to the web version of this article.)

growth (no deformation) or closing (slight deformation).

Fig. 12d shows that the overall changes in backscattering over fast ice regions are small between the two images. Most of the spatial patterns (i.e., spatial relative changes of backscattering coefficient) are the same in both images, while only the absolute value of gray tones changes to a certain degree. With regard to the effect of incidence angles, if the local incidence angle differences are over 5°, relatively strong changes in the backscattering coefficient should be observed to some extent, dependent on the dominant scattering mechanism (e.g., surface scattering from smooth or rough ice or volume scattering) (Makynen et al., 2002). The differences in the incidence angles of the SAR image pairs used in this study approximately range from about 1.5° to 3°. Backscattering changes are about 0.5 dB on average with a maximum of about 1.5 dB, which are not so significant considering that there could be some changes on snow structure on sea ice. As a supplement, the incidence angle was not identified as a particularly important variable when it was added to the set of input variables (Fig. B2 of Appendix B). This would indicate that the proposed models can be used to detect fast ice regions using bitemporal SAR images at a 5-day interval with similar incidence angle configurations, especially when the differences in incidence angles are not significant.

Antarctic sea ice chart data were used to evaluate the reliability of fast ice detection models using object-based SAR data. Sea ice chart data obtained at 15 November 2010 for the fast ice region of the Bellingshausen Sea sector were available. The ice chart superimposed

on a model detection result is shown in Fig. 13. The visual comparison shows a good agreement but a difference at the top right of the scene. In a closer examination of the two SAR images (Fig. 13a–b), the movements of icebergs trapped in sea ice, the occurrence of openings by leads, and several rectilinear or wedge-shaped cracks were clearly confirmed. The reason for the difference may be attributed to the length of the time interval used to derive fast ice. Previous studies explain that using a longer time interval over fast ice tends to detect smaller fast ice areas due to a lower likelihood that the ice would remain spatially stationary for the entire period, whereas using a shorter time interval can confuse temporarily frozen drift ice as fast ice. A relatively long time interval (e.g., 20 days) has been used as a tradeoff (Fraser et al., 2010), but generally, it is due to data availability constraints by a long revisit time of satellite sensor systems especially for optical sensor and InSAR data. The bi-weekly Antarctic sea ice chart defined a slightly wider area as fast ice despite using a longer time interval than this study. Although the two data with different time intervals have different physical definitions, they show fairly consistent results.

4. Conclusions

This study showed that bi-temporal L-band ALOS PALSAR SAR images with a short time interval (i.e., 5 days) are capable of identifying Antarctic fast ice. This study suggested an algorithm that combines image segmentation, image correlation analysis, and machine learning
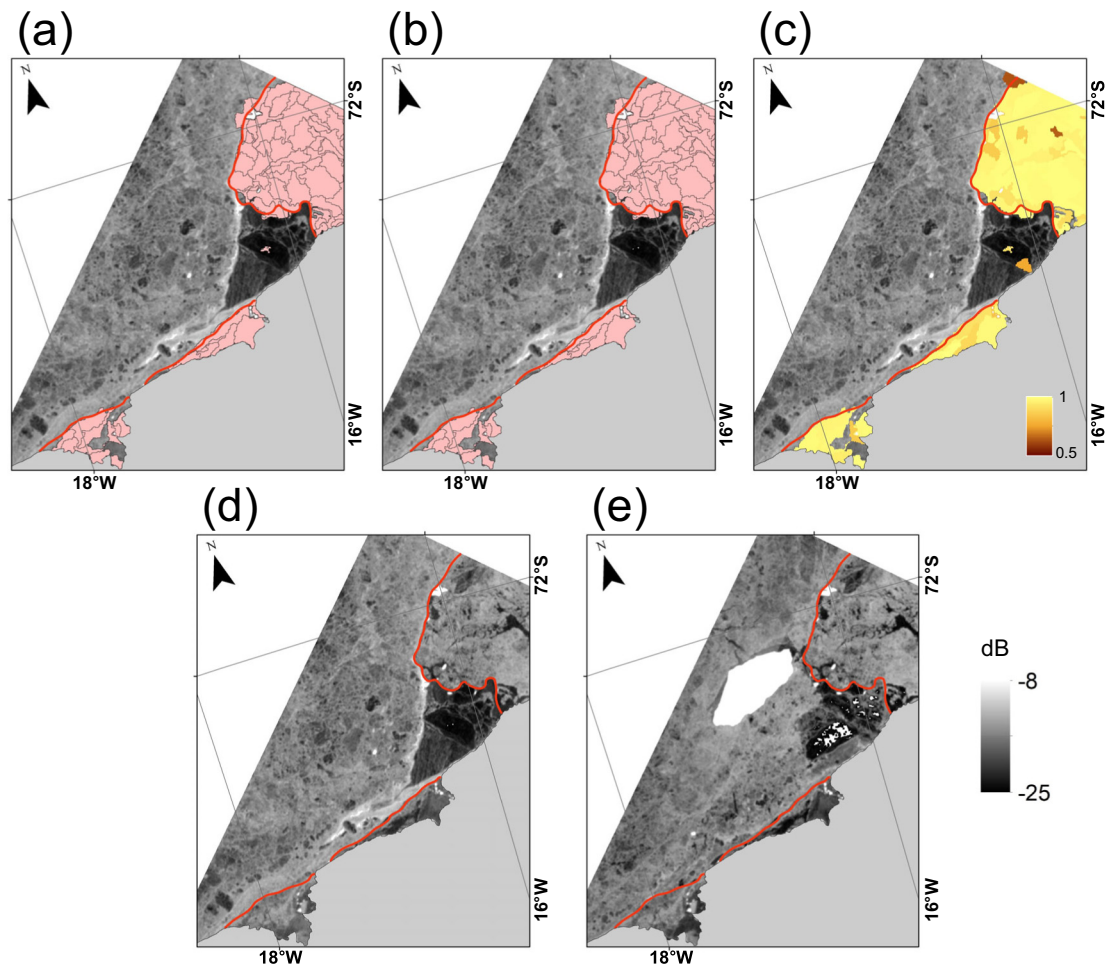
Fig. 10. Landfast sea ice detection results off the Brunt ice shelf, eastern Weddell Sea of (a) random forest (RF), (b) extremely randomized trees (ERT), (c) logistic regression (LR) models, (d) backscatter image of L-band HH-pol ALOS PALSAR for date 1 (8 Aug. 2007), and (e) backscatter image for date 2 (13 Aug. 2007). Red solid lines indicate the reference fast ice edge, RF and ERT results are shown in pink color and LR result for the probability of fast ice coverage in yellowish-starched color, and gray areas are both Antarctic continent and ice shelves. (For interpretation of the references to color in this figure legend, the reader is referred to the web version of this article.)

techniques to detect fast ice regions. The proposed object-based approach was well suited to high resolution SAR images by extracting spatially homogeneous fast ice regions. Fast ice does not move much over time, so it was possible to identify fast ice areas that are highly correlated between the two temporally separated satellite images compared to pack ice regions. In addition, the fast ice detection method using SAR images provides an opportunity to study the rapidly changing interaction between fast ice and pack ice on a regional scale in more detail.

The model performance results for the validation data show that all three methods yield high accuracy. Marginally misclassified or undetected fast ice cases occurred in unstable areas, which are generally affected by the surrounding environment at the edge of fast ice. Correlation and STD of backscatter were identified as the most important and contributing variables for detecting fast ice. This coincides with the physical characteristics of fast ice with little motion over time and spatial homogeneity, including the fast ice properties.

The results for test data which are not included in training from the West Antarctic ocean sectors show that the proposed approach achieved good performance without significant misclassifications or missing objects. Some misclassifications over the fast ice region could be because the L-band is sensitive to snow cover to some extent, or some places in the region might have thinner ice that is slightly deformed during either ice growth (no deformation) or closing (slight

deformation) between both image dates. Heavy snow load on the ice could be an error source for some misclassification as well. In addition, very old multi-year fast ice was identified as an error source for misclassification as it has higher backscatter when compared to other fast ice regions. The results compared with various reference data confirm the robustness and reliability of the proposed algorithm particularly using L-band ALOS PALSAR SAR images. We expect this algorithm to be suitable for fast ice detection in different regions, especially when the local incidence angle differences are not so significant.

We have extracted fast ice regions in a short time interval (i.e., 5 days) using spatially overlapping SAR images (considering small differences in incidence angles) regardless of repeat cycles. Fast ice detection conducted in earlier studies was limited to a longer time interval (e.g. 20 days in Fraser et al. (2010)). As a future study, it would be interesting to compare the method with existing methods in East Antarctica that use a longer time span such as 20 days.

This study is limited to the L-band ALOS PALSAR data and covers the early melt (i.e., early November) and freeze up (i.e., June to August) periods in the Antarctic, except for summer season (i.e., December to February) due to no data available. Thus, it is not possible to generalize the proposed model directly using other SAR images due to the different characteristics of other bands to sea ice or different seasons. It would also be interested in the investigation on the utility of L-band SAR for fast ice detection over other popularly used frequencies (e.g. C-band, X-
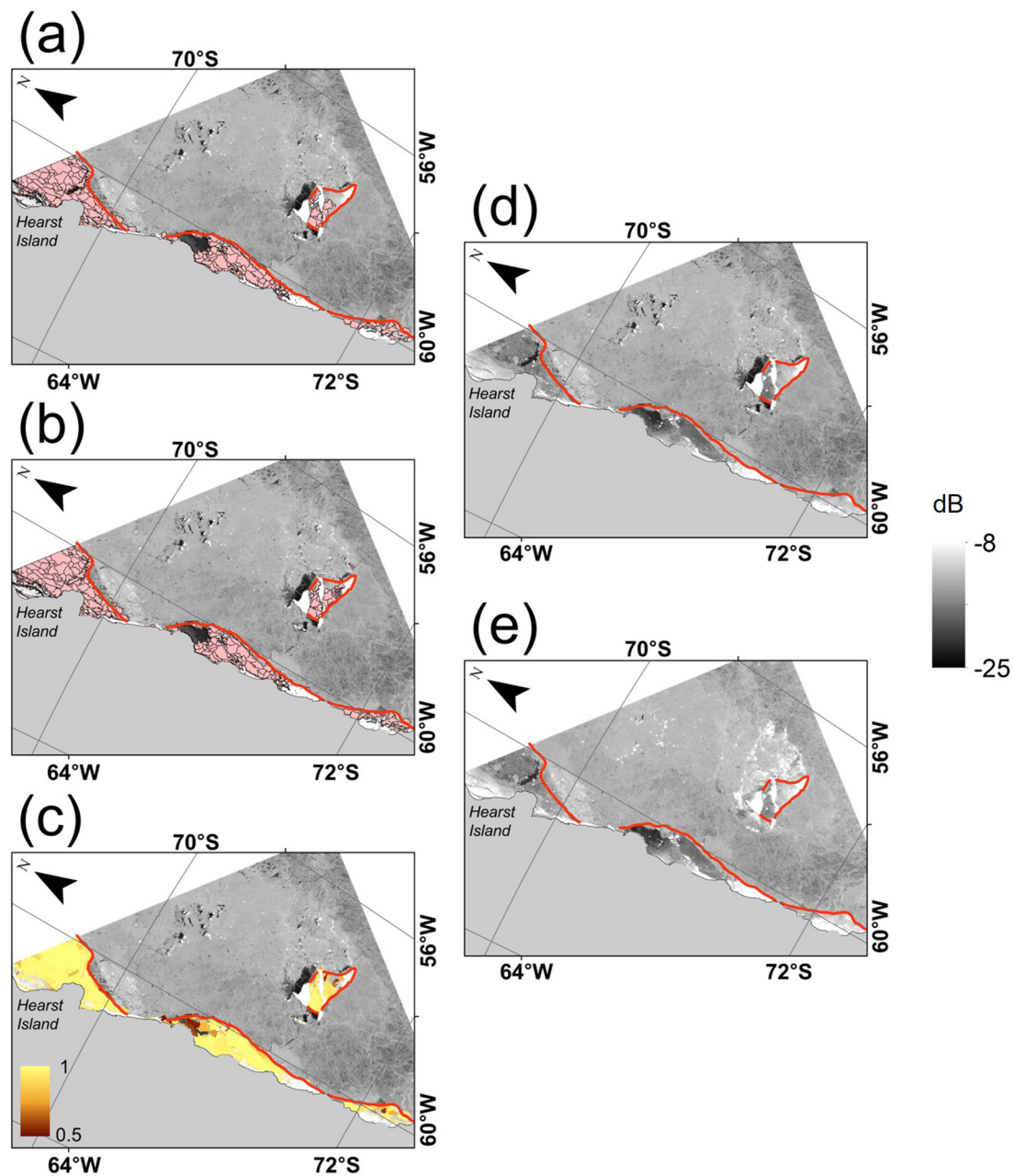
Fig. 11. Landfast sea ice detection results off the Larsen ice shelf, Antarctic Peninsula of (a) random forest (RF), (b) extremely randomized trees (ERT), (c) logistic regression (LR) models, (d) backscatter image of L-band HH-pol ALOS PALSAR for date 1 (20 Aug. 2007), and (e) backscatter image for date 2 (25 Aug. 2007). Red solid lines indicate the reference fast ice edge, RF and ERT results are shown in pink color and LR result for the probability of fast ice coverage in yellowish-starched color, and gray areas are both Antarctic continent and ice shelves. For the zoomed images for fast ice regions near the Hearst Island, please refer to Fig. B1 in Appendix B. (For interpretation of the references to color in this figure legend, the reader is referred to the web version of this article.)

band, and Ku-band). However, it might require a new training process for machine learning with other SAR data. In future research, using combinations of different polarization images from RADARSAT-2 and PALSAR-2, for example, could provide more plentiful information on different scattering mechanisms depending on sea ice properties.

With regard to producing a large-scale fast ice product based on this technique, it could be feasible if all the steps were automated, including SAR image processing, compositing image pairs, segmentation for the composite images, calculating input variables and applying a machine learning model. Cloud-based computing environments such as Google Earth Engine and Amazon Web Services would allow for implementing the processes.

CRediT authorship contribution statement

Miae Kim: Conceptualization, Methodology, Visualization, Formal analysis, Investigation, Writing - original draft, Software. **Hyun-Cheol Kim:** Writing - review & editing, Resources, Funding acquisition. **Jungho Im:** Conceptualization, Methodology, Investigation, Supervision, Writing - review & editing. **Sanggyun Lee:** Software, Writing - review & editing. **Hyangsun Han:** Writing - review & editing.

Declaration of competing interest

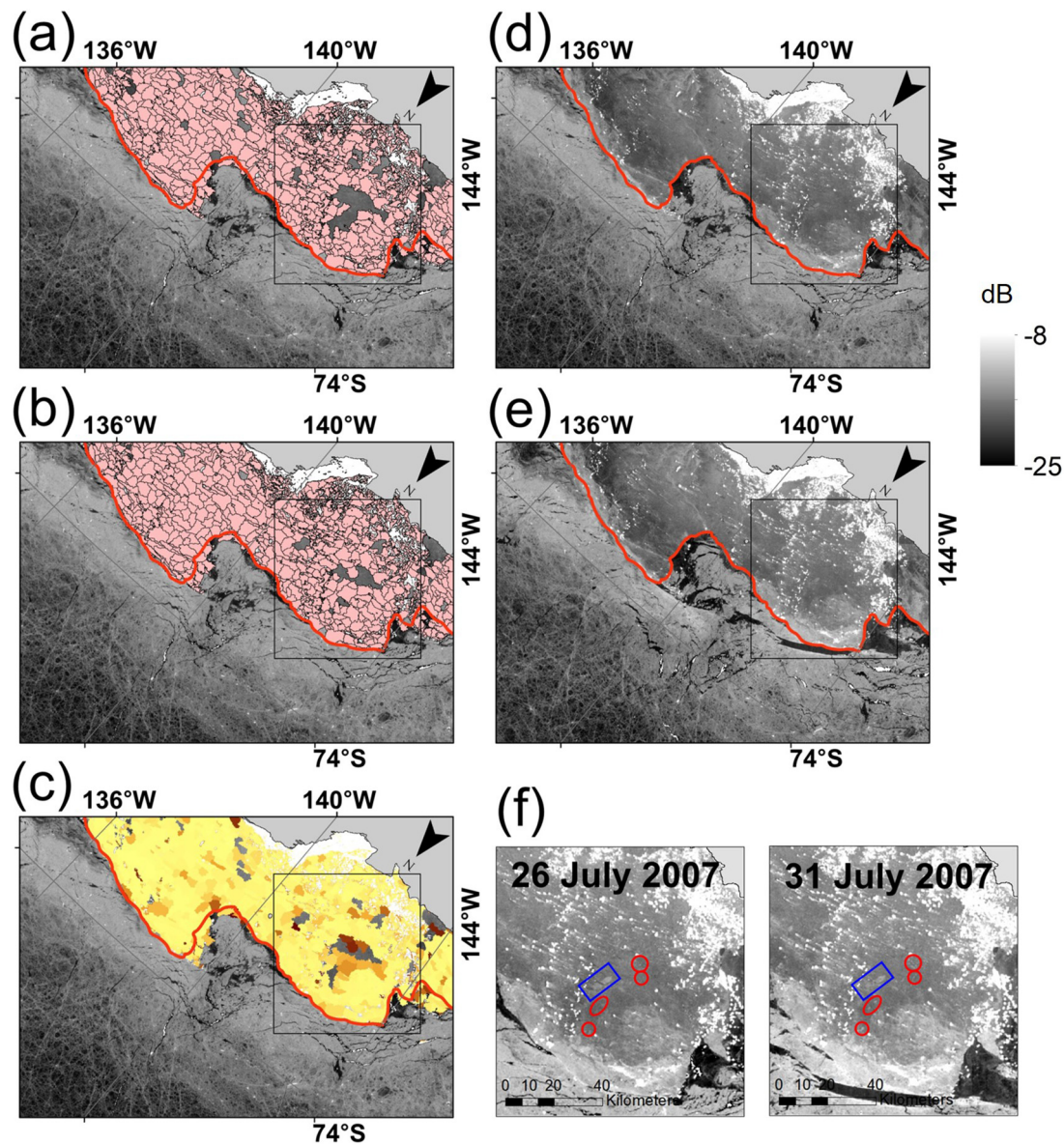The authors declare that they have no known competing financial

Fig. 12. Landfast sea ice detection results off the Nickerson ice shelf, eastern Ross Sea of (a) random forest (RF), (b) extremely randomized trees (ERT), (c) logistic regression (LR) models, (d) backscatter image of L-band HH-pol ALOS PALSAR for date 1 (26 July 2007), and (e) backscatter image for date 2 (31 July 2007), and (f) a closer view for the misclassified fast ice region (solid black line box) with red circles and a floe in the blue rectangular box that show some changes in the backscattering between both images. Red solid lines indicate the reference fast ice edge, RF and ERT results are shown in pink color and LR result for the probability of fast ice coverage in yellowish-starched color, and gray areas are both Antarctic continent and ice shelves. (For interpretation of the references to color in this figure legend, the reader is referred to the web version of this article.)

interests or personal relationships that could have appeared to influence the work reported in this paper.

Appendix A. Segmentation process in eCognition software

The multiresolution segmentation algorithm in eCognition was used, which is a bottom-up segmentation method that minimizes the heterogeneity of image objects and maximizes homogeneity to obtain the best segmentation results (Belgiu and Drăguţ, 2014). Segmentation starts with single pixels and repeatedly merges them into larger groups by using certain user-defined criteria for homogeneity (Chen et al., 2018; Lu and He, 2018; Han et al., 2018). The segmentation procedure iterates until each image object finds the best neighbor to merge with based on several user-defined segmentation criteria with three parameters (i.e., scale, shape, and compactness; Witharana and Civco, 2014). First, the scale parameter
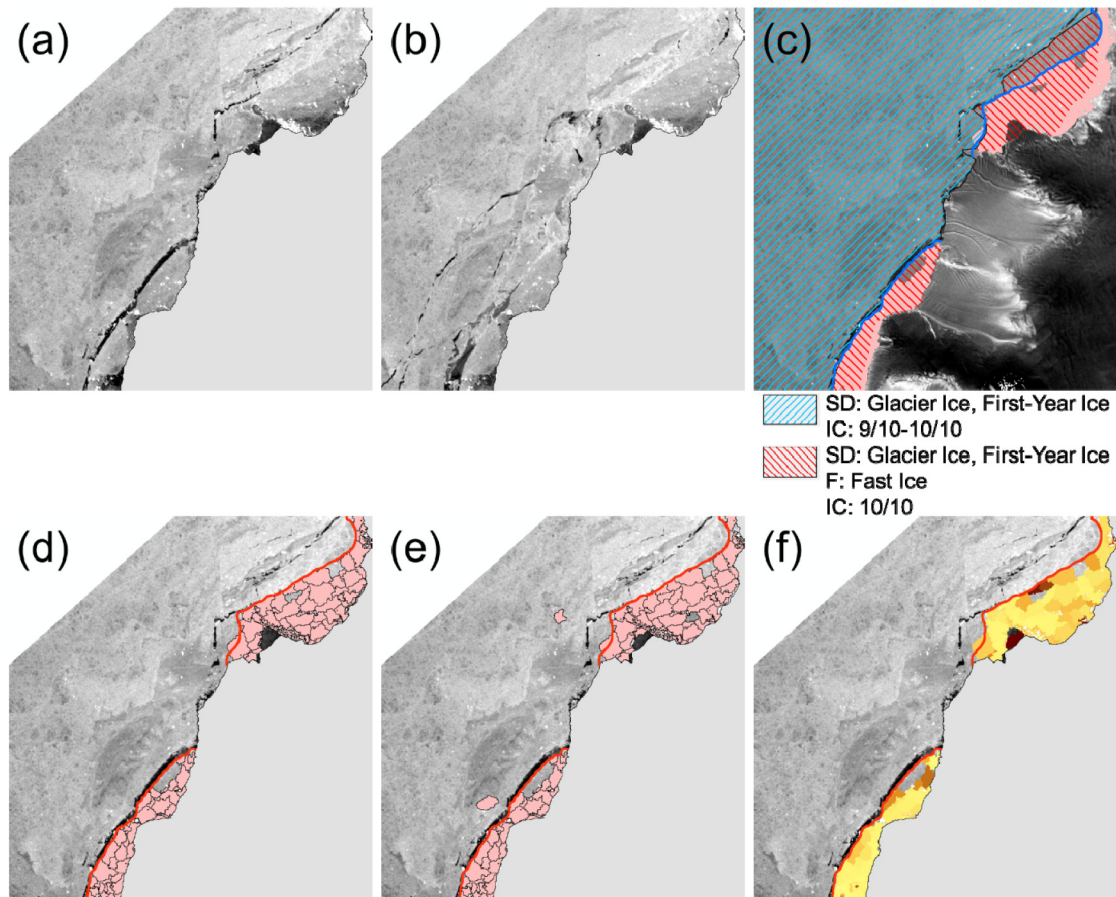
Fig. 13. Qualitative analysis results. (a) Backscatter image of L-band HH-pol ALOS PALSAR for date 1; (b) backscatter for date 2; (c) comparison between the Antarctic Ice Chart and RF result (pink area). The light blue and red hatched areas are from the Antarctic Ice Chart. SD, F, IC are abbreviations for ice chart codes meaning Stage of Development, Form of ice, and sea Ice Concentration, respectively. The blue solid line is fast ice edge as a reference. (d–f) Results of machine learning models (RF, ERT, LR, respectively) with fast ice edge as a reference (red solid line). Gray areas are both Antarctic continent and ice shelves. The color bar for backscatter images is the same as those used in Figs. 9–12. (For interpretation of the references to color in this figure legend, the reader is referred to the web version of this article.)

influences the size of resultant objects. In homogeneous areas of images, objects will be larger than those in images with heterogeneous surfaces. It also limits the maximum allowable criteria of the following homogeneity. Secondly, the color (i.e., pixel values) and shape parameters are used for the homogeneity criteria. As these are complementary criteria, they have a relationship of Color = 1 – Shape. As the value of the shape criterion increases, images are segmented for spatial homogeneity. Eventually, the relationship will determine the degree of the contribution of the spectral values of images for object generation. The shape parameter cannot be greater than 0.9 in order for the resulting objects to be somewhat segmented based on their backscatter values. It is also adjusted by the smoothness and compactness parameters. By changing the value of the compactness field, the smoothness criterion is defined, which then determines the degree of smoothness or compactness among the objects. The compactness parameter is calculated as the ratio of the perimeter of an object and its area. The more compact an object is, the smaller its border length is (i.e., pixels in an object are closer to the circle boundary). This is useful for images where compact and non-compact objects are not clearly distinguishable due to weak spectral contrast (Yan et al., 2006). The compactness criterion can enhance the quality of segmentation for strongly textured data such as radar backscatter images with highly fractured objects (Lucieer and Lamarche, 2011).
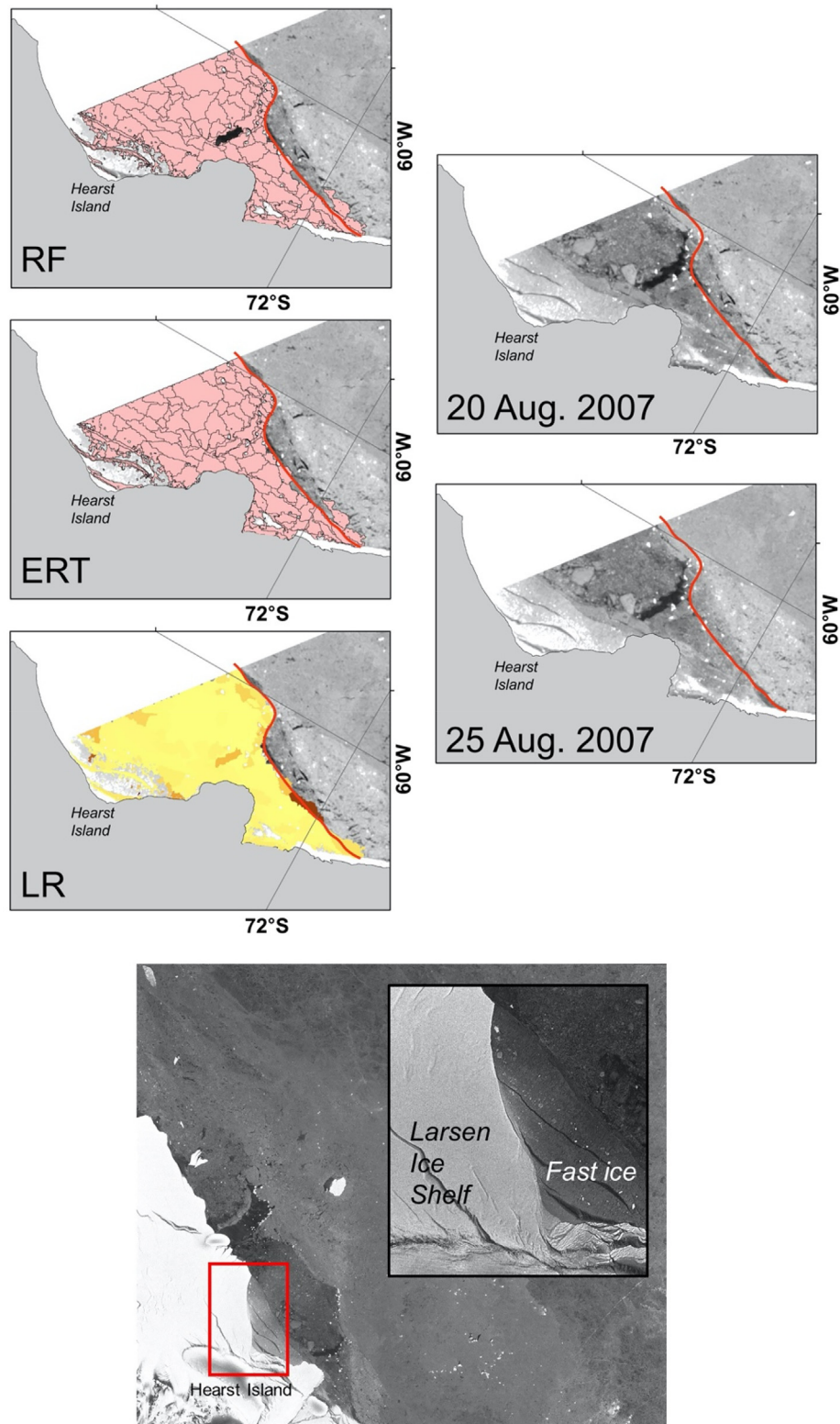
Appendix B

Fig. B1. Upper: Landfast sea ice detection results zoomed into the Hearst Island area for each model and corresponding backscatter images of L-band HH-pol ALOS PALSAR for date 1 and 2. Red solid lines indicate the reference fast ice edge, RF and ERT results are shown in pink color and LR result for the probability of fast ice coverage in yellowish-starched color, and gray areas are both Antarctic continent and ice shelves. Bottom: ALOS PALSAR images of wide beam mode on 25th August 2007 (back) and fine beam mode with a spatial resolution of 10 m on 11 December 2007 (front) over multi-year land fast sea ice off the Larsen Ice Shelf, Antarctic Peninsula.
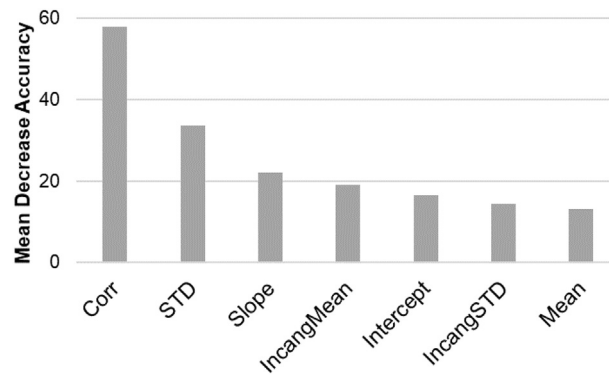
Fig. B2. Relative variable importance indicated by mean decrease accuracy of random forest by adding incidence angle variables (i.e., IncangMean and IncangSTD, which were obtained from the mean and standard deviation of incidence angle for each object).

References

Amani, M., Salehi, B., Mahdavi, S., Granger, J., Brisco, B., 2017. Wetland classification in Newfoundland and Labrador using multi-source SAR and optical data integration. GIScience & remote sensing 54, 779–796.

Barrett, B., Nitze, I., Green, S., Cawkwell, F., 2014. Assessment of multi-temporal, multi-sensor radar and ancillary spatial data for grasslands monitoring in Ireland using machine learning approaches. Remote Sens. Environ. 152, 109–124.

Barry, R., Moritz, R.E., Rogers, J., 1979. The fast ice regimes of the Beaufort and Chukchi Sea coasts, Alaska. Cold Reg. Sci. Technol. 1, 129–152.

Belgiu, M., Drăguţ, L., 2014. Comparing supervised and unsupervised multiresolution segmentation approaches for extracting buildings from very high resolution imagery. ISPRS J. Photogramm. Remote Sens. 96, 67–75.

Bintanja, R., Van Oldenborgh, G., Drijfhout, S., Wouters, B., Katsman, C., 2013. Important role for ocean warming and increased ice-shelf melt in Antarctic sea-ice expansion. Nat. Geosci. 6, 376–379.

Breiman, L., 2001. Random forests. Mach. Learn. 45, 5–32.

Casey, J.A., Howell, S.E., Tivy, A., Haas, C., 2016. Separability of sea ice types from wide swath C-and L-band synthetic aperture radar imagery acquired during the melt season. Remote Sens. Environ. 174, 314–328.

Cavalieri, D., Parkinson, C., 2008. Antarctic sea ice variability and trends, 1979–2006. Journal of Geophysical Research: Oceans 113.

Chen, G., Weng, Q., Hay, G., He, Y., 2018. Geographic object-based image analysis (GEOBIA): emerging trends and future opportunities. GIScience and Remote Sensing 55, 159–182.

Comiso, J.C., Steffen, K., 2001. Studies of Antarctic sea ice concentrations from satellite data and their applications. Journal of Geophysical Research: Oceans 106, 31361–31385.

Comiso, J.C., Gersten, R.A., Stock, L.V., Turner, J., Perez, G.J., Cho, K., 2017. Positive trend in the Antarctic sea ice cover and associated changes in surface temperature. J. Clim. 30, 2251–2267.

Cook, A.J., Vaughan, D.G., 2010. Overview of areal changes of the ice shelves on the Antarctic Peninsula over the past 50 years. Cryosphere 4, 77–98.

Dammann, D.O., Eicken, H., Meyer, F.J., Mahoney, A.R., 2016. Assessing small-scale deformation and stability of landfast sea ice on seasonal timescales through L-band SAR interferometry and inverse modeling. Remote Sens. Environ. 187, 492–504.

Dammann, D.O., Eriksson, L.E., Mahoney, A.R., Eicken, H., Meyer, F.J., 2019. Mapping pan-Arctic landfast sea ice stability using Sentinel-1 interferometry. Cryosphere 13, 557–577.

Developer, E, 2012. Trimble eCognition Developer 8.7 Reference Book. Trimble Germany GmbH, Munich.

Dierking, W., Busche, T., 2006. Sea ice monitoring by L-band SAR: an assessment based on literature and comparisons of JERS-1 and ERS-1 imagery. IEEE Trans. Geosci. Remote Sens. 44, 957–970.

Fraser, A.D., Massom, R.A., Michael, K.J., 2010. Generation of high-resolution East Antarctic landfast sea-ice maps from cloud-free MODIS satellite composite imagery. Remote Sens. Environ. 114, 2888–2896.

Fraser, A.D., Massom, R.A., Michael, K.J., Galton-Fenzi, B.K., Lieser, J.L., 2012. East Antarctic landfast sea ice distribution and variability, 2000–08. J. Clim. 25, 1137–1156.

Fraser, A.D., Ohshima, K.I., Nihashi, S., Massom, R.A., Tamura, T., Nakata, K., Williams, G.D., Carpentier, S., Willmes, S., 2019. Landfast ice controls on sea-ice production in the Cape Darnley Polynya: a case study. Remote Sens. Environ. 233, 111315.

Geurts, P., Ernst, D., Wehenkel, L., 2006. Extremely randomized trees. Mach. Learn. 63, 3–42.

Giles, A., Massom, R., Heil, P., Hyland, G., 2011. Semi-automated feature-tracking of East Antarctic sea ice from Envisat ASAR imagery. Remote Sens. Environ. 115, 2267–2276.

Giles, A.B., Massom, R.A., Lytle, V.I., 2008. Fast-ice distribution in East Antarctica during 1997 and 1999 determined using RADARSAT data. Journal of Geophysical Research: Oceans 113.

Han, H., Kim, Y., Jin, H., Lee, H., 2015. Analysis of annual variability of landfast sea ice near Jangbogo Antarctic Station using InSAR coherence images. Korean Journal of Remote Sensing 31, 501–512.

Han, M., Zhang, C., Zhou, Y., 2018. Object-wise joint-classification change detection for remote sensing images based on entropy query-by fuzzy ARTMAP. GIScience and Remote Sensing 55, 265–284.

Heil, P., 2006. Atmospheric conditions and fast ice at Davis, East Antarctica: a case study. Journal of Geophysical Research: Oceans 111.

Howell, S.E., Komarov, A.S., Dabboor, M., Montpetit, B., Brady, M., Scharien, R.K., Mahmud, M.S., Nandan, V., Geldsetzer, T., Yackel, J.J., 2018. Comparing L-and C-band synthetic aperture radar estimates of sea ice motion over different ice regimes. Remote Sens. Environ. 204, 380–391.

Im, J., Jensen, J.R., 2005. A change detection model based on neighborhood correlation image analysis and decision tree classification. Remote Sens. Environ. 99, 326–340.

Im, J., Jensen, J., Tullis, J., 2008. Object-based change detection using correlation image analysis and image segmentation. Int. J. Remote Sens. 29, 399–423.

Jang, E., Im, J., Park, G.-H., Park, Y.-G., 2017. Estimation of fugacity of carbon dioxide in the East Sea using in situ measurements and geostationary ocean color imager satellite data. Remote Sens. 9, 821.

Johansen, K., Sallam, N., Robson, A., Samson, P., Chandler, K., Derby, L., Eaton, A., Jennings, J., 2018. Using GeoEye-1 imagery for multi-temporal object-based detection of Canegrub damage in sugarcane fields in Queensland, Australia. GIScience and Remote Sensing 55, 285–305.

Karvonen, J., 2018. Estimation of Arctic land-fast ice cover based on dual-polarized Sentinel-1 SAR imagery. Cryosphere 12 (8), 2595.

Karvonen, J.A., 2004. Baltic sea ice SAR segmentation and classification using modified pulse-coupled neural networks. IEEE Trans. Geosci. Remote Sens. 42, 1566–1574.

Kern, S., Ozsoy-Çiçek, B., Worby, A.P., 2016. Antarctic sea-ice thickness retrieval from ICESat: inter-comparison of different approaches. Remote Sens. 8, 538.

Kim, M., Im, J., Han, H., Kim, J., Lee, S., Shin, M., Kim, H.-C., 2015. Landfast sea ice monitoring using multisensor fusion in the Antarctic. GIScience & remote sensing 52, 239–256.

Kim, M., Im, J., Park, H., Park, S., Lee, M.-I., Ahn, M.-H., 2017. Detection of tropical overshooting cloud tops using Himawari-8 imagery. Remote Sens. 9, 685.

Komarov, A.S., Buehner, M., 2019. Detection of first-year and multi-year sea ice from dual-polarization SAR images under cold conditions. IEEE Trans. Geosci. Remote Sens. 57 (11), 9109–9123.

Kurtz, N., Markus, T., 2012. Satellite observations of Antarctic sea ice thickness and volume. Journal of Geophysical Research: Oceans 117.

Lang, W., Zhang, P., Wu, J., Shen, Y., Yang, X., 2016. Incidence angle correction of SAR sea ice data based on locally linear mapping. IEEE Trans. Geosci. Remote Sens. 54, 3188–3199.

Lee, H., Yuan, T., Jung, H.C., Beighley, E., 2015. Mapping wetland water depths over the central Congo Basin using PALSAR ScanSAR, Envisat altimetry, and MODIS VCF data. Remote Sens. Environ. 159, 70–79.

Lee, S., Han, H., Im, J., Jang, E., Lee, M., 2017. Detection of deterministic and probabilistic convection initiation using Himawari-8 Advanced Himawari Imager data. Atmospheric Measurement Techniques 10, 1859–1864.

Li, X., Ouyang, L., Hui, F., Cheng, X., Shokr, M., Heil, P., 2018. An improved automated method to detect landfast ice edge off Zhongshan Station using SAR imagery. IEEE Journal of Selected Topics in Applied Earth Observations and Remote Sensing 11, 4737–4746.

Liaw, A., Wiener, M., 2002. Classification and regression by randomForest. R news 2, 18–22.

Liu, H., Guo, H., Zhang, L., 2015. SVM-based sea ice classification using textural features and concentration from RADARSAT-2 Dual-Pol ScanSAR data. IEEE Journal of Selected Topics in Applied Earth Observations and Remote Sensing 8, 1601–1613.

Liu, T., Abd-Elrahman, A., Morton, J., Wilhelm, V., 2018. Comparing fully convolutional networks, random forest, support vector machine, and patch-based deep convolutional neural networks for object-based wetland mapping using images from small unmanned aircraft system. GIScience and Remote Sensing 55, 243–264.

Lu, B., He, Y., 2018. Optimal spatial resolution of Unmanned Aerial Vehicle (UAV)-

acquired imagery for species classification in a heterogeneous grassland ecosystem. GIScience and Remote Sensing 55, 205–220.

Lucieer, V., Lamarche, G., 2011. Unsupervised fuzzy classification and object-based image analysis of multibeam data to map deep water substrates, Cook Strait, New Zealand. Cont. Shelf Res. 31 (11), 1236–1247.

Mahmud, M.S., Geldsetzer, T., Howell, S.E., Yackel, J.J., Nandan, V., Scharien, R.K., 2018. Incidence angle dependence of HH-polarized C-and L-band wintertime backscatter over Arctic Sea ice. IEEE Trans. Geosci. Remote Sens. 56, 6686–6698.

Mahoney, A., Eicken, H., Graves, A., Shapiro, L., Cotter, P., 2004. Landfast sea ice extent and variability in the Alaskan Arctic derived from SAR imagery. In: Geoscience and Remote Sensing Symposium, 2004. IGARSS'04. Proceedings. 2004 IEEE International. IEEE, pp. 2146–2149.

Mahoney, A., Eicken, H., Shapiro, L., Graves, A., 2006. Defining and locating the seaward landfast ice edge in northern Alaska. In: 18th International Conference on Port and Ocean Engineering under Arctic Conditions (POAC'05), Potsdam, NY, pp. 991–1001.

Mahoney, A.R., Eicken, H., Gaylord, A.G., Gens, R., 2014. Landfast sea ice extent in the Chukchi and Beaufort seas: the annual cycle and decadal variability. Cold Reg. Sci. Technol. 103, 41–56.

Makynen, M., Manninen, A.T., Simila, M., Karvonen, J.A., Hallikainen, M.T., 2002. Incidence angle dependence of the statistical properties of C-band HH-polarization backscattering signatures of the Baltic Sea ice. IEEE Trans. Geosci. Remote Sens. 40, 2593–2605.

Massom, R., Hill, K., Lytle, V., Worby, A., Paget, M., Allison, I., 2001. Effects of regional fast-ice and iceberg distributions on the behaviour of the Mertz Glacier polynya, East Antarctica. Ann. Glaciol. 33, 391–398.

Massom, R.A., Drinkwater, M.R., Haas, C., 1997. Winter snow cover on sea ice in the Weddell Sea. Journal of Geophysical Research: Oceans 102, 1101–1117.

Massom, R.A., Hill, K., Barbraud, C., Adams, N., Ancel, A., Emmerson, L., Pook, M.J., 2009. Fast ice distribution in Adélie Land, East Antarctica: interannual variability and implications for emperor penguins Aptenodytes forsteri. Mar. Ecol. Prog. Ser. 374, 243–257.

Massom, R.A., Giles, A.B., Fricker, H.A., Warner, R.C., Legrésy, B., Hyland, G., Young, N., Fraser, A.D., 2010. Examining the interaction between multi-year landfast sea ice and the Mertz Glacier Tongue, East Antarctica: another factor in ice sheet stability. Journal of Geophysical Research: Oceans 115.

Mazur, A., Wåhlin, A., Krężel, A., 2017. An object-based SAR image iceberg detection algorithm applied to the Amundsen Sea. Remote Sens. Environ. 189, 67–83.

McLaren, K., McIntyre, K., Prospere, K., 2019. Using the random forest algorithm to integrate hydroacoustic data with satellite images to improve the mapping of shallow nearshore benthic features in a marine protected area in Jamaica. GIScience and Remote Sensing 56, 1065–1092.

Meyer, F.J., Mahoney, A.R., Eicken, H., Denny, C.L., Druckenmiller, H.C., Hendricks, S., 2011. Mapping arctic landfast ice extent using L-band synthetic aperture radar interferometry. Remote Sens. Environ. 115, 3029–3043.

Murphy, E.J., Clarke, A., Symon, C., Priddle, J., 1995. Temporal variation in Antarctic sea-ice: analysis of a long term fast-ice record from the South Orkney Islands. Deep-Sea Res. I Oceanogr. Res. Pap. 42, 1045–1062.

Mutowo, G., Mutanga, O., Masocha, M., 2019. Including shaded leaves in a sample affects the accuracy of remotely estimating foliar nitrogen. GIScience and Remote Sensing 56, 1114–1127.

Nihashi, S., Ohshima, K.I., 2015. Circumpolar mapping of Antarctic coastal polynyas and landfast sea ice: relationship and variability. J. Clim. 28, 3650–3670.

Normile, D., 2015. Antarctic researchers ponder challenges posed by increasing sea ice. http://www.sciencemag.org/news/2015/05/antarctic-researchers-ponder-challenges-posed-increasing-sea-ice, Accessed date: 30 September 2017.

Ohshima, K.I., Fukamachi, Y., Williams, G.D., Nihashi, S., Roquet, F., Kitade, Y., Tamura, T., Hirano, D., Herraiz-Borreguero, L., Field, I., 2013. Antarctic Bottom Water production by intense sea-ice formation in the Cape Darnley polynya. Nat. Geosci. 6, 235.

Parkinson, C., Cavalieri, D., 2012. Antarctic sea ice variability and trends, 1979–2010. Cryosphere 6, 871.

Parkinson, C.L., DiGirolamo, N.E., 2016. New visualizations highlight new information on the contrasting Arctic and Antarctic sea-ice trends since the late 1970s. Remote Sens. Environ. 183, 198–204.

Price, D., Rack, W., Haas, C., Langhorne, P.J., Marsh, O., 2013. Sea ice freeboard in McMurdo Sound, Antarctica, derived by surface-validated ICESat laser altimeter data. Journal of Geophysical Research: Oceans 118, 3634–3650.

Ressel, R., Frost, A., Lehner, S., 2015. A neural network-based classification for sea ice types on X-band SAR images. IEEE Journal of Selected Topics in Applied Earth Observations and Remote Sensing 8, 3672–3680.

Rhee, J., Im, J., 2017. Meteorological drought forecasting for ungauged areas based on machine learning: using long-range climate forecast and remote sensing data. Agric.

For. Meteorol. 237, 105–122.

Richardson, H.J., Hill, D.J., Denesiuk, D.R., Fraser, L.H., 2017. A comparison of geographic datasets and field measurements to model soil carbon using random forests and stepwise regressions (British Columbia, Canada). GIScience & remote sensing 54, 573–591.

Scott, R.C., Lubin, D., Vogelmann, A.M., Kato, S., 2017. West Antarctic Ice Sheet cloud cover and surface radiation budget from NASA A-train satellites. J. Clim. 30, 6151–6170.

Simmonds, I., 2015. Comparing and contrasting the behaviour of Arctic and Antarctic sea ice over the 35 year period 1979–2013. Ann. Glaciol. 56, 18–28.

Sonobe, R., Yamaya, Y., Tani, H., Wang, X., Kobayashi, N., Mochizuki, K.-i., 2017. Assessing the suitability of data from Sentinel-1A and 2A for crop classification. GIScience & remote sensing 54, 918–938.

Spinhirne, J.D., Palm, S.P., Hart, W.D., Hlavka, D.L., Welton, E.J., 2005. Cloud and aerosol measurements from GLAS: overview and initial results. Geophys. Res. Lett. 32.

Stammerjohn, S., Martinson, D., Smith, R., Yuan, X., Rind, D., 2008. Trends in Antarctic annual sea ice retreat and advance and their relation to El Niño–Southern Oscillation and Southern Annular Mode variability. Journal of Geophysical Research: Oceans 113.

Suen, J.Y., Fang, M.T., Lubin, P.M., 2014. Global distribution of water vapor and cloud cover—sites for high-performance THz applications. IEEE Transactions on Terahertz Science and Technology 4, 86–100.

Tamura, T., Ohshima, K.I., Nihashi, S., 2008. Mapping of sea ice production for Antarctic coastal polynyas. Geophys. Res. Lett. 35.

Turner, J., Phillips, T., Marshall, G.J., Hosking, J.S., Pope, J.O., Bracegirdle, T.J., Deb, P., 2017. Unprecedented springtime retreat of Antarctic sea ice in 2016. Geophys. Res. Lett. 44, 6868–6875.

Ushio, S., 2006. Factors affecting fast-ice break-up frequency in Lützow-Holm Bay, Antarctica. Ann. Glaciol. 44, 177–182.

Viñas, M.-J., 2017. Sea ice extent sinks to record lows at both poles. https://www.nasa.gov/feature/goddard/2017/sea-ice-extent-sinks-to-record-lows-at-both-poles, Accessed date: 30 September 2017.

Wang, L., Scott, K.A., Xu, L., Clausi, D.A., 2016. Sea ice concentration estimation during melt from dual-pol SAR scenes using deep convolutional neural networks: a case study. IEEE Trans. Geosci. Remote Sens. 54, 4524–4533.

Wesche, C., Dierking, W., 2012. Iceberg signatures and detection in SAR images in two test regions of the Weddell Sea, Antarctica. J. Glaciol. 58, 325–339.

Wesche, C., Dierking, W., 2015. Near-coastal circum-Antarctic iceberg size distributions determined from Synthetic Aperture Radar images. Remote Sens. Environ. 156, 561–569.

Williams, R., Rees, W., Young, N., 1999. A technique for the identification and analysis of icebergs in synthetic aperture radar images of Antarctica. Int. J. Remote Sens. 20, 3183–3199.

Witharana, C., Civco, D.L., 2014. Optimizing multi-resolution segmentation scale using empirical methods: exploring the sensitivity of the supervised discrepancy measure Euclidean distance 2 (ED2). ISPRS J. Photogramm. Remote Sens. 87, 108–121.

WMO, 2014. World Meteorological Organization Sea Ice Nomenclature, Volume 1 terminology. In: WMO Report No. 259, . http://www.aari.ru/gdsidb/xml/wmo_259.php.

Wylie, B., Pastick, N., Picotte, J., Deering, C., 2019. Geospatial data mining for digital raster mapping. GIScience and Remote Sensing 56, 406–429.

Xie, H., Tekeli, A.E., Ackley, S.F., Yi, D., Zwally, H.J., 2013. Sea ice thickness estimations from ICESat Altimetry over the Bellingshausen and Amundsen Seas, 2003–2009. Journal of Geophysical Research: Oceans 118, 2438–2453.

Yan, G., Mas, J.F., Maathuis, B.H.P., Xiangmin, Z., Van Dijk, P.M., 2006. Comparison of pixel-based and object-oriented image classification approaches—a case study in a coal fire area, Wuda, Inner Mongolia, China. Int. J. Remote Sens. 27 (18), 4039–4055.

Yang, Y., Zhijun, L., Leppäranta, M., Cheng, B., Shi, L., Lei, R., 2016. Modelling the thickness of landfast sea ice in Prydz Bay, East Antarctica. Antarct. Sci. 28, 59–70.

Yoo, S., Im, J., Wagner, J., 2012. Variable selection for hedonic model using machine learning approaches: a case study in Onondaga County, NY. Landsc. Urban Plan. 107, 293–306.

Zakhvatkina, N.Y., Alexandrov, V.Y., Johannessen, O.M., Sandven, S., Frolov, I.Y., 2013. Classification of sea ice types in ENVISAT synthetic aperture radar images. IEEE Trans. Geosci. Remote Sens. 51, 2587–2600.

Zwally, H.J., Comiso, J.C., Parkinson, C.L., Campbell, W.J., Carsey, F.D., 1983. Antarctic Sea Ice, 1973–1976: Satellite Passive-Microwave Observations. National Aeronautics And Space Administration, Washington DC.

Zwally, H.J., Comiso, J.C., Parkinson, C.L., Cavalieri, D., Gloersen, P., 2002. Variability of Antarctic sea ice 1979–1998. Journal of Geophysical Research: Oceans 107.